Clear Roads, Clear Vision: Advancements in Multi-Weather Restoration for Smart Transportation

Vijay M. Galshetwar, Praful Hambarde, Prashant W. Patil, Akshay Dudhane, Sachin Chaudhary, Santosh Kumar Vipparathi, and Subrahmanyam Murala

Abstract*—Adverse weather conditions such as haze, rain, and snow significantly degrade the quality of images and videos, posing serious challenges to intelligent transportation systems (ITS) that rely on visual input. These degradations affect critical applications including autonomous driving, traffic monitoring, and surveillance. This survey presents a comprehensive review of image and video restoration techniques developed to mitigate weather-induced visual impairments. We categorize existing approaches into traditional prior-based methods and modern data-driven models, including CNNs, transformers, diffusion models, and emerging vision-language models (VLMs). Restoration strategies are further classified based on their scope: single-task models, multi-task/multi-weather systems, and all-in-one frameworks capable of handling diverse degradations. In addition, we discuss day and night time restoration challenges, benchmark datasets, and evaluation protocols. The survey concludes with an in-depth discussion on limitations in current research and outlines future directions such as mixed/compound-degradation restoration, real-time deployment, and agentic AI frameworks. This work aims to serve as a valuable reference for advancing weather-resilient vision systems in smart transportation environments. Lastly, to stay current with rapid advancements in this field, we will maintain regular updates of the latest relevant papers and their open-source implementations at *https://github.com/ChaudharyUPES/A-comprehensive-review-on-Multi-weather-restoration**

***Index Terms*—Multi-weather restoration, All-weather Surveillance, Transportation, Traffic monitoring.**

I. Introduction

In modern intelligent transportation systems (ITS), computer vision plays a pivotal role in enabling tasks such as lane detection, object tracking, autonomous driving, traffic monitoring, and autonomous navigation. These systems rely heavily on the clarity and reliability of visual data captured by on-board cameras and roadside infrastructure. However, in real-world outdoor environments, visual degradation due to adverse weather such as haze, rain, snow, and fog, significantly impairs scene understanding, leading to reduced accuracy in downstream perception tasks and increased risk in safety-critical applications [1]–[3]. These adverse weather conditions introduce various forms of degradation like reduced visibility, occlusion, noise, and distortions, that obscure critical scene details and hinder the performance of downstream vision algorithms [1]. Hazy conditions, caused by atmospheric scattering, degrade visibility and color fidelity; rain introduces streaks and blur that affect feature detection and motion estimation; and snow leads to occlusions and texture-like noise that confuse segmentation and classification systems. Figure 1 shows real-world degradations under day and night-time conditions [4], [5]. Each weather type introduces distinct statistical distortions, posing a challenge for models to generalize across diverse scenarios.

Figure 1: Real-world haze, rain, and snow degradations in daytime and nighttime images.

Hence, visibility improvement also known as multi-weather image/video restoration has become a critical pre-processing step for ensuring the robustness of transportation infrastructure under real-world conditions. It refers to the process of reconstructing clear images or videos from degraded ones affected by haze, rain, snow, or other atmospheric conditions [1], [2], [6]–[12]. Traditional image restoration techniques primarily rely on atmospheric scattering models and handcrafted priors [13], [14]. While these methods are effective in constrained environments, they often fail to generalize across complex and dynamic real-world settings. Recently, deep learning-based approaches using convolutional neural networks (CNNs) [1], [15], [16], generative adversarial networks (GANs) [17], [18], transformers [19], knowledge distillation [20], domain transla-

Vijay M. Galshetwar is with the Finolex Academy of Management and Technology, Ratnagiri, Maharashtra, India (e-mail: vijay.galshetwar@famt.ac.in).
Praful Hambarde is with Drone Lab, Centre for Artificial Intelligence and Robotics, Indian Institute of Technology Mandi, India (e-mail: praful@iitmandi.ac.in).
Prashant W. Patil is with the Mehta Family School of Data Science and Artificial Intelligence, Indian Institute of Technology Guwahati, India (e-mail: pwpatil@iitg.ac.in).
Akshay Dudhane is with the Computer Vision Department, MBZUAI, Abu Dhabi, United Arab Emirates (e-mail: akshay.dudhane@mbzuai.ac.ae).
Sachin Chaudhary is with the School of Computer Science, UPES Dehradun, India. (E-mail: sachin.chaudhary@ddn.upes.ac.in).
Santosh Kumar Vipparathi is with the Department of Electrical Engineering, Indian Institute of Technology Ropar, India (e-mail: skvipparathi@iitrpr.ac.in).
Subrahmanyam Murala is with School of Computer Science and Statistics, Trinity College Dublin, Dublin, Ireland (e-mail: muralas@tcd.ie).

tion [21], multimodal prompt learning [12], and diffusion models [22] have shown significant success in learning complex weather-specific patterns and restoring visibility across a range of adverse conditions. Some of the significant applications and current challenges in multi-weather restoration are given below:

A. Significance of Multi-weather Restoration in ITS

- **Enhancing driver assistance systems:** In autonomous driving, restoration techniques enhance visibility in bad weather, ensuring reliable visual data. [7], [8], [23].
- **Improving transportation monitoring:** In a traffic monitoring center, especially in areas affected by severe weather, restored video quality is essential for ensuring the security and the functionality of the systems [23], [11].
- **Airport and port operations:** Image restoration improves runway visibility for air traffic control and ensures clear visuals for safe vessel docking and navigation [11].

B. Major Challenges of Multi-weather Restoration:

A major challenge in multi-weather restoration research is the limited availability of real-world datasets due to safety, cost, and environmental constraints. Consequently, synthetic datasets are commonly used to simulate weather conditions. Figure 2 illustrates the synthetic formation of haze, rain, and snow, providing controlled scenarios for model development. Some of the other challenges are as given below:

- **Complex and mixed weather conditions:** Real-world scenes often involve combinations of fog, rain, and snow, making restoration more complex [24]–[26].
- **Task interference in multi-task learning:** Simultaneous learning of multiple restoration tasks can lead to performance trade-offs [6].
- **Computational efficiency:** Real-time requirements for ITS demand lightweight and efficient models [1].
- **Lack of diverse and high-quality datasets:** Synthetic datasets often lack real-world diversity [12].
- **Underexplored multi-weather video restoration:** Despite advances in image restoration, video-based methods remain largely unexplored, except few attempts [8], [27].

This survey presents a comprehensive review of state-of-the-art (SOTA) methods in multi-weather image and video restoration, focusing on the tasks of de-hazing, de-raining, and de-snowing. We categorize prior-based and learning-based approaches, including unified models that address multiple degradations. Moreover, we highlight their relevance to smart transportation applications, where robust visibility is essential for reliable decision-making.

Our key contributions are as follows:

- Provide a comprehensive overview of existing methodologies and techniques for image/video de-hazing, de-raining, de-snowing, multi-weather and all-in-one restoration.
- Summarize SOTA approaches, including prior-based models, learning-based methods, and hybrid techniques.

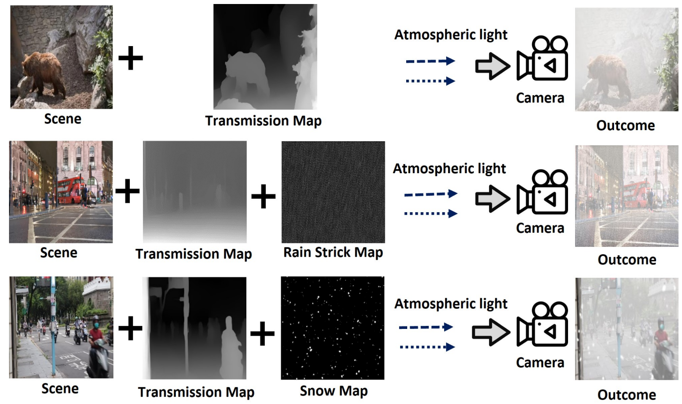

Figure 2: Synthetic image generation pipeline: atmospheric light settings combine with (i) a transmission map for depth-dependent haze, (ii) rain-streak overlays for rain, and (iii) snow-particle maps for snow, producing realistic hazy, rainy, and snowy scenes.

- Discussed evaluation metrics and benchmark datasets relevant to image/video restoration in ITS.
- Identify current challenges and open research directions for advancing multi-weather restoration algorithms.

By presenting this comprehensive overview, we aim to support researchers and practitioners in driving forward the development of robust, weather-resilient vision systems tailored for next-generation smart transportation applications.

II. Related Work

The literature on restoration techniques is categorized into five main areas: haze, rain, snow, all-in-one, and multi-weather restoration approaches. This section gives an overview of the first three categories *i.e. weather specific*, including traditional and learning-based approaches. The detailed review of existing multi-weather restoration and all-in-one approaches is provided in Sections III and IV, respectively. Figure 3 illustrates a timeline of major image/video restoration methods.

A. De-hazing Approaches

The formation of synthetic hazy image using atmospheric scattering model [28] as: $I_x(n) = J_x(n) \cdot T_x(n) + A \cdot (1 - T_x(n))$ where, $I_x(n)$ and $J_x(n)$ are the hazy and haze-free images at pixel x and time n respectively, A is the atmospheric light, and $T_x(n)$ is scene transmission map of the image estimated as $T_x(n) = e^{(-\beta d(x))}$, where, β denotes attenuation coefficient and $d(x)$ denotes depth of the scene.

1) Image De-hazing: Major categories are as below:
Prior-based Methods: Wang *et al.* [29] proposed a physical-model-based de-hazing technique using the dark channel prior (DCP) with atmospheric light estimation. They later enhanced it with a multi-scale retinex and color restoration scheme [30]. Other notable methods include linear transformation [31], detail manipulation [32], and confidence priors [33] to improve performance in complex scenes. A unified model for bridging haze scenarios was also introduced in [34], offering improved generalization and stability.

Filter based Methods: A multi-scale correlated wavelet approach is proposed by Liu *et al.* [35] for simultaneous de-hazing and denoising. A globally guided image filtering technique was introduced by Li *et al.* [36] for contrast enhancement and high-quality restoration. Ma *et al.* [37], improved color channel transfer and multiexposure fusion with k-means clustering were employed for effective de-hazing.
Markov Random Field Based Methods: Tan *et al.* [38] developed a cost function in the framework of Markov random fields which can be efficiently optimized by various techniques, such as graph-cuts or belief propagation.
Learning-based Methods: Galdran *et al.* [39] proposed a variational de-hazing framework, while Cai *et al.* [40] introduced a CNN-based end-to-end method. Liu *et al.* [41] designed an attention-driven multi-scale network for fast and accurate de-hazing. Dudhane *et al.* [10] developed a varicolored network to restore color balance in hazy images.

Zhang *et al.* proposed several strategies, including a pyramid channel-based framework [42] and a multi-level feature enhancement method [15]. Zhu *et al.* [43] introduced a multi-exposure fusion technique, while Shyam *et al.* [44] focused on domain-invariant de-hazing. Bai *et al.* [45] proposed a progressive feature refinement strategy. Additionally, Dudhane *et al.* introduced a deep fusion network [46] and a residual inception-based GAN model [47] for improved de-hazing performance. Yu *et al.* [48] proposed a visible-infrared fusion approach for enhanced visibility.

Beyond paired data settings, Engin *et al.* [49] adopted an unpaired training scheme using CycleGAN for flexible de-hazing. Zhu *et al.* [50] incorporated the atmospheric scattering model into a GAN framework to improve visual quality. Dudhane *et al.* [51] introduced single image de-hazing using unpaired adversarial training. Ren *et al.* [52] further refined the process by incorporating holistic edge information with multi-scale CNN. Wang *et al.* [53] proposed TMS-GAN to mitigate domain shifts between synthetic and real-world hazy images. Wang *et al.* [54] developed a cycle spectral normalized soft likelihood estimation patch GAN for haze removal, while Manu *et al.* [55] presented GANID for high-contrast, color-preserving de-hazing across natural and synthetic datasets. Song *et al.* [56] proposed DehazeFormer that consists of modified normalization layer, activation function, and spatial information aggregation scheme. Further, Liu *et al.* [57] developed a self-enhancement GAN algorithm incorporating depth estimation. Li *et al.* [58] approached de-hazing as a two-way image translation problem using a weakly supervised framework. Along with homogeneous de-hazing, authors introduced with a Self-paced Semi-Curricular attention Network by Guo *et al.* [59] and image processing network by Kim *et al.* [60] for non-homogeneous de-hazing. All these above methods are purely trained with synthetically generated data, which limits the performance on real-world hazy data. Wei *et al.* [61] presented a robust unpaired image de-hazing approach with adversarial deformation constraints to align hazy and clean image distributions. Fu *et al.* [62] proposed IPC-Dehaze is an iterative predictor-critic code decoding for real-world image de-hazing. Liu *et al.* [63] presented a novel variational nighttime de-hazing framework using hybrid regularization that enhances the perceptual visibility of nighttime hazy scene. Li *et al.* [64] proposed a semi-supervised learning network for image de-hazing that combines synthetic and real-world hazy images, enhancing the model's generalization through supervised and unsupervised techniques. Cong *et al.* [65] introduced a semi-supervised nighttime de-hazing method with spatial-frequency awareness and realistic brightness constraints.
Wu *et al.* [66] developed a compact single-image de-hazing network utilizing contrastive learning. Yang *et al.* [67] introduced a self-augmented unpaired de-hazing method that uses density and depth decomposition, addressing limitations in synthetic paired training data requirement. Ding *et al.* [68] developed a unified de-hazing and denoising network using DCP with an edge-aware network. Wei *et al.* [61] introduced an adversarial deformation constraint for robust unpaired image de-hazing. Wang *et al.* [69] developed an unsupervised contrastive learning framework that trains on unpaired clean and hazy images.

2) Video De-hazing: Major categories are as below:
Prior-Based Methods: Park *et al.* [70] introduced a video de-hazing system leveraging fast airlight estimation and the DCP to maintain temporal coherence across frames, improving video quality and visibility. Dong *et al.* [71] developed an adaptive DCP method that incorporates spatial-temporal correlations for real-time traffic video de-hazing. Adidela *et al.* [72] consolidated state-of-the-art DCP-based techniques for both single-image and video de-hazing. Wu *et al.* [73] proposed a real-time HD video defogging approach using a modified DCP algorithm, tailored for high-definition content and suitable for immediate application. The artifacts issue is tackled in Li *et al.* [74] with gradient and color prior regularization and Ashwini *et al.* [75] with improved gradient preservation. Some contrast enhancement methods like segments videos into view-based clusters Yu *et al.* [76], transmission estimation using the HSL color model Soma *et al.* [77], physical priors and temporal information across video frames Xu *et al.* [78] and dual-transmission-map Auoub *et al.* [79] are proposed.
Markov Random Field based Methods: Zhang *et al.* [80] and Cai *et al.* [81] presented the haze-free video model by assuming frame-by-frame video sequences for improving temporal coherence utilizing Markov Random Field and optical flow.
Retinex Theory Based Methods: Xue *et al.* [82] introduced a video de-hazing algorithm that utilizes Multi-Scale Retinex with Color Restoration.
Learning-based Methods: Fan xue [16] introduced a semi-supervised video de-hazing method leveraging CNNs and a dynamic haze generator. Galshetwar *et al.* proposed various approaches for video de-hazing primarily focusing on computational complexity and temporal consistency aspect [83]–[86].
Non-homogeneous Methods: Ancuti *et al.* [87] reported on the NTIRE 2023 HR nonhomogeneous de-hazing challenge, showcasing advancements and benchmarking state-of-the-art methods for high-resolution videos with complex haze distributions. Liu *et al.* [88] emphasized the quality assessment of video enhancement techniques in the same challenge, offering a detailed evaluation framework for nonhomogeneous de-hazing and encouraging the development of more robust de-hazing algorithms.

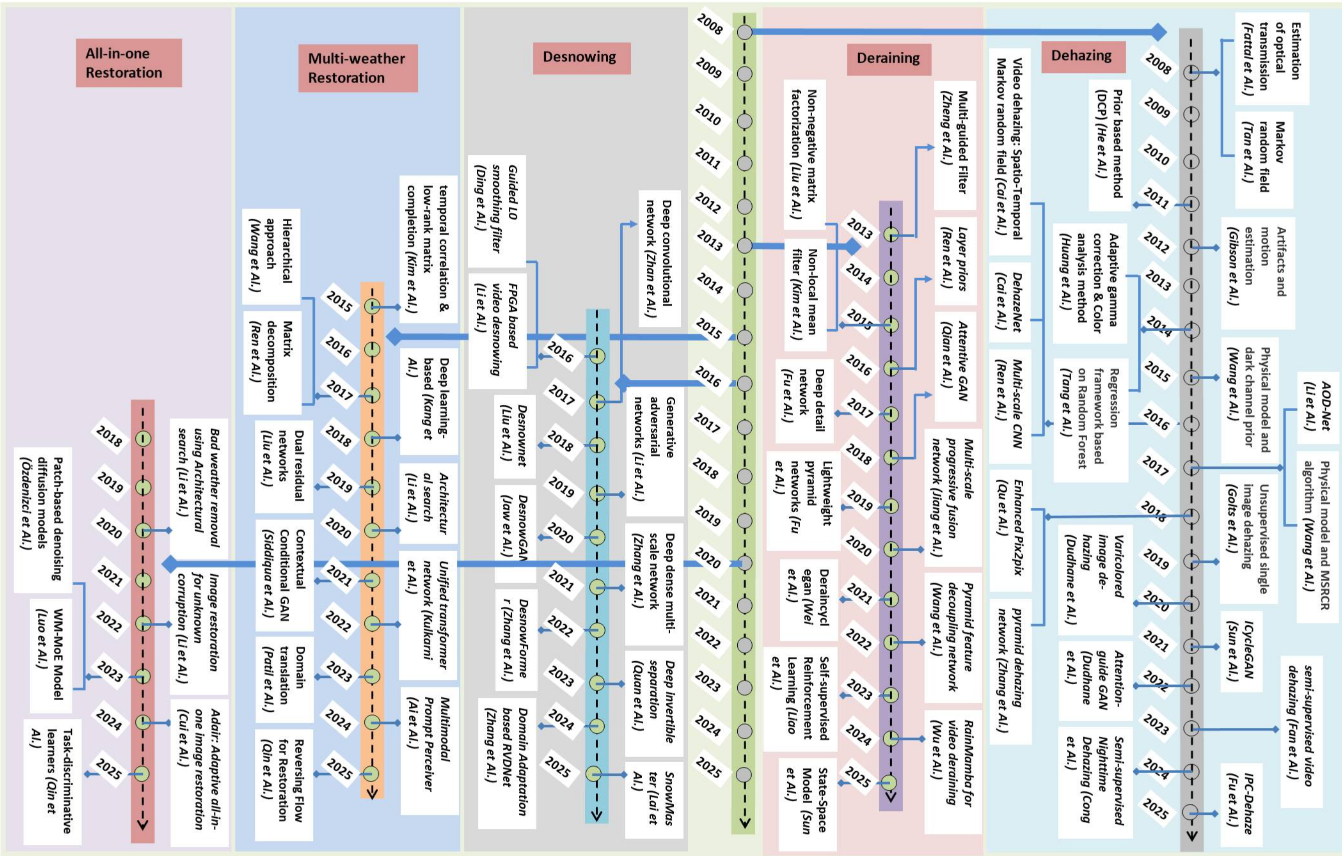

Figure 3: The development timeline of hazy, rainy, snowy and multi-weather degraded image/video restoration approaches.

B. De-raining Approaches

For supervised training, getting rainy and rain-free images is difficult. Therefore, researchers started training the supervised models with synthetic data provided in Yang *et al.* [89]. Mathematically, the rainy data is generated as:

$$O_t = B_t + S_t, \qquad t = 1, 2, ..., N \tag{1}$$

where, S_t represents rain streaks of t^{th} frame, B_t represent the t^{th} rain-free frame, O_t is the t^{th} synthetically generated rainy frame and t is the temporal indicator, N denotes the number of video frames. With the introduction of rain accumulation and accumulation flow the above equation is expressed as:

$$O_t = T_t B_t + (1 - T_t) A_t + U_t + S_t, \qquad t = 1, 2, ..., N. \tag{2}$$

where, A_t is the global atmospheric light, T_t is atmospheric transmission map, U_t is rain accumulation flow layer based on atmospheric flow and local raindrop density.

$$O'_t = (1 - \alpha_t)(B_t + S_t) + \alpha_t R_t \tag{3}$$

where, α_t is an alpha matting map, and R_t is the rain reliance map. Using Eq. 1-3, rain model with occlusion is given as:

$$O'_t = (1 - \alpha_t)(O_t) + \alpha_t R_t \tag{4}$$

Hence, Eq. 4 represents a rain model that captures rain streaks, accumulation, accumulation flow, and occlusions in a comprehensive way [89].

1) Image De-raining: Major categories are as below:

Prior-based Methods: Luo *et al.* [90] introduced a discriminative sparse coding approach that utilizes dictionary learning to separate rain streaks from the background, preserving image details effectively. Li *et al.* [91] proposed a layer-based model using priors to guide the separation of rain streaks as a distinct layer. Focusing on gradient domain analysis, [92] presented a method that decorrelates rain streaks and background by leveraging the differential impact of rain streaks on the X- and Y-gradients of an image, producing visually clear outputs.

Filter Based Methods: [93] proposed a multi-frame de-raining algorithm that employs a motion-compensated non-local mean filter to enhance rain removal in dynamic video scenes. [94] introduced a guided filtering to preserve background textures and edges, making it suitable for real-time use. For static images, [95] developed a guided filter-based approach to reduce noise from rain and snow particles.

Matrix Decomposition Based Methods: [96] introduced a matrix decomposition-based method for video de-snowing and de-raining, which can also be applied to single images. [97] proposed a rain removal method using non-negative matrix factorization (NMF) for single images.

Learning-based Methods: Li *et al.* [98] introduced a recurrent squeeze-and-excitation context aggregation network for image de-raining. A context aggregation based network is proposed in [99]. Jiang *et al.* [100] developed a multi-scale progressive fusion network to refine images at multiple scales for rain streak removal. Yang *et al.* [101] proposed a deep joint rain detection and removal framework that employs a CNN to detect and eliminate rain streaks simultaneously. A adversarial learning-based approaches are proposed [102], [103] for image de-raining. Fu *et al.* [104] introduced lightweight Laplacian pyramid decomposition network for image de-raining to achieve high-quality results with low computational complexity. Further, the pyramid feature decoupling network is proposed in [105], which enhances image clarity by decoupling multi-scale features. Xiao *et al.* [106] proposed the Image De-raining Transformer, that incorporates general priors of vision tasks, such as locality and hierarchy, into the network design. Li *et al.* [107] presented image de-raining via similarity diversity model for single traffic. For lane detection and depth estimation, Li *et al.* [108] proposed a ultra-fast de-raining plugin for vision-based perception of autonomous driving.

2) Video De-raining: *Prior-based Methods:* [93] proposed a multi-frame de-raining algorithm using a motion-compensated non-local mean filter for rainy video sequences. [94] introduced a method to Utilize local phase information to remove rain from video. Islam *et al.* [109] proposed a video de-raining considering the visual properties of rain streaks.
Learning-based Methods: Mi *et al.* [110] developed an image fusion-based video de-raining method using sparse representation. A progressive subtractive recurrent lightweight network is proposed in [111]. Further, multi-patch progressive neural network is presented in [112]. Semi-supervised approach with dynamical rain generator is proposed in [113]. Yang *et al.* [114] proposed a two-stage recurrent network with dual-level flow regularizations to perform the inverse recovery process of the rain synthesis model. Yan *et al.* [115] proposed a self-alignment network with transmission-depth consistency. Wang *et al.* [116] presented a novel approach by integrating a bio-inspired event camera into the unsupervised video de-raining pipeline, which captures high temporal resolution information and model complex rain characteristics. A hybrid transformer with global and local representations is developed in [117]. Lin *et al.* [118] introduced nighttime video de-raining method with adaptive rain removal and adaptive correction. Wu *et al.* [119] proposed an improved state space models based video de-raining network (RainMamba) with a novel Hilbert scanning mechanism to capture sequence level local information. Semi-supervised state-space model with dynamic stacking filter is proposed by Sun *et al.* [120] for real-world video de-raining.

C. De-snowing Approaches

The de-snowing model training and evaluation is based on synthetic dataset as getting paired clean and snowy data is difficult [121]. The synthetic data is generated as:

$$\alpha(x) = \begin{cases} \sigma\left(-\left(V(x)-\gamma\right)\times\beta\right), & if\ daytime \\ \sigma\left(\left(V(x)-\gamma\right)\times\beta\right), & if\ nighttime \end{cases} \quad (5)$$

[121] first convert the RGB image to the HSV color space, where V = max(R, G, B) represents the largest color component. v denotes the value of the V channel in the HSV space, which is normalized to the range of 0 to 1. γ and β are adjusted based on the specific video, and σ represents the softmax function. The formation of snowy video is as below:

where *Aug* denotes data augmentation. *Z* is the final output with both snow and haze.

1) Image De-snowing: Major categories are as below.
Prior-based Methods: Zhang *et al.* [122] proposed a deep dense multi-scale network for snow removal, utilizing semantic and depth priors to enhance image quality. A hierarchical dual-tree complex wavelet representation and contradict channel loss is proposed in [123] to improve the performance.
Filter Based Methods: A guided smoothing filter was proposed in [124] for single image rain and snow removal. In [125], a supervised median filtering scheme was introduced for marine snow removal. A snowfall model smoothing filter that preserves edge features was presented in [126].
FPGA Based Methods: [127] presented an FPGA-based snow removal approach capable of real-time processing for images with a minimum resolution of 640×480, demonstrating the practicality of hardware-accelerated de-snowing solutions.
Learning-based Methods: Zhan *et al.* [128] employed a CNN to distinguish clouds from snow in satellite imagery. A perceptual generative adversarial network (GAN) for single-image de-snowing was proposed in [17]. Subsequent GAN-based methods introduced compositional [129] and two-stage architectures [130] for more effective snow removal. Transformer-based architectures have also been proposed, incorporating global context [131], multi-scale projection [132], and context interaction [133]. A deep invertible separation method was introduced in [134] for single image de-snowing. In [135], a SnowMaster framework was proposed for real-world de-snowing using MLLM with multi-model feedback optimization.

2) Video De-snowing: Major de-snowing approaches are discussed below. *Prior-based Methods:* A depth prior-based stable tensor decomposition method for video snow removal was introduced in [136], incorporating semantic and geometric priors. In [137], a saliency-guided approach using dual adaptive spatiotemporal filtering and guided filtering was proposed.
Learning-based Methods: [138] introduced RVDNet, a two-stage network for real-world video de-snowing with domain adaptation, improving the performance of video snow removal. Video de-snowing remains underexplored, often addressed alongside other weather effects like rain or haze.

III. Multi-weather Image/Video Restoration

This section discusses multi-weather (multi-task) image and video restoration approaches. Most of the existing methods are task-wise fine-tuned and evaluated across multiple weather (tasks) conditions. We discuss task-specific fine-tuned models evaluated on de-hazing, de-raining, and de-snowing tasks.

A. Image Restoration

Prior-based Methods: [13] introduced a hierarchical approach for rain and snow removal from single color images. [139] developed a joint framework for degraded image restoration and simultaneous localization processes.
Learning-based Methods: Chen *et al.* [140] introduced leveraging gated context aggregation for haze and rain removal. A dual-tree complex wavelet fusion based approach is proposed in [141] for rain and snow removal. Zaamir *et al.* [142]

introduced a multi-stage network, that progressively acquires restoration functions for the degraded inputs. In [143], a memory replay training strategy is adapted for multi-weather (*haze, rain and snow*) image restoration. Zaamir *et al.* [144] proposed restoration transformer by designing multi-head attention and feed-forward network for restoration. Wang *et al.* [145] presented Uformer, an effective and efficient Transformer-based encoder-decoder architecture for image restoration. zhou *et al.* [146] proposed a fourier spatial interaction modeling and Fourier channel evolution for image restoration. Gao *et al.* [147] proposed a frequency-oriented transformer excelling in weather-degraded image restoration. A transformer with grid-based feature fusion [148] and degradation-aware [2] approaches are proposed for multi-weather image restoration. First semi-supervised learning framework based on vision-language model is proposed in [149]. Qin *et al.* [150] presented ResFlow: a image restoration framework that models the degradation process as a deterministic path using continuous normalizing flows. Kulkarni *et al.* [9] proposed WiperNet, a computationally efficient deep-learning model designed to restore degraded images under adverse weather conditions such as haze, rain, and snow. By leveraging lightweight architecture and optimized feature extraction techniques, WiperNet delivers enhanced visibility and scene clarity while maintaining low computational overhead. Kulkarni *et al.* [1] introduces a lightweight model designed to enhance images degraded by various weather conditions, such as rain and snow. The network is computationally efficient having only 1.1 million parameters. However, it provides limited generalization to extreme conditions like dense fog or heavy rainstorms. A domain translation-based framework in [21] restores images degraded by various weather conditions by generating weather-specific variants from a single input. While effective, it adds pipeline complexity, computational overhead, and increases the risk of error propagation.

B. Video Restoration

Prior-based Methods: In [96] Matrix decomposition is proposed for video de-snowing and de-raining, using a weighted average approach. In [14] highlighted the role of nature-based solutions for climate adaptation, focusing on restoring environments affected by weather conditions.
Matrix Decomposition Based Methods: Kim *et al.* [151] proposed a video de-raining and de-snowing algorithm that leverages temporal correlation and low-rank matrix completion.
Learning-based Methods: A consolidated adversarial network for video de-raining and de-hazing task is proposed in [152]. In [8], the authors emphasized meta-adaptation techniques for video de-hazing and de-raining under veiling effects in data-scarce scenarios. A dual-frame spatio-temporal feature modulation framework is proposed in [153] to address degradation from diverse weather conditions. Above discussed methods achieve significant performance for multi-weather degraded image restoration. However, there are many challenging aspects where future work may rely on.

- Multi-weather restoration models must adaptively handle diverse real-world degradations, including varying rain and snow intensities and non-uniform haze.
- The model should minimize computational load; trainable parameters, inference time, model size, and FLOPs—for real-time multi-weather restoration.
- Despite progress in multi-weather image restoration, advancements in video restoration remain limited.

IV. All-in-One Image Restoration

The emergence of all-in-one image restoration models represents a major advancement in handling multiple visual degradations, such as haze, noise, blur, low-light, rain, smog, and snow within a single unified framework. These models are trained once on a combined dataset and deployed across various adverse conditions without task-specific fine-tuning. This generalization capability makes them particularly valuable for intelligent transportation systems, where consistent, real-time visual clarity is crucial across diverse weather scenarios. With the scope of this survey, we focus on existing all-in-one approaches targeting key degradations, including haze, rain, noise, and snow. We categorize recent all-in-one methods based on their architectural principles.

A. Prompt-Based and Adaptive Architectures

Prompt-based methods have emerged as a flexible approach to guide restoration processes across diverse degradation types. For instance, PromptIR [191] introduces degradation-specific prompts that modulate the restoration network, enabling effective handling of de-hazing, denoising, and de-raining tasks within a single model. Building upon this, Adaptive Blind All-in-One Restoration (ABAIR) [192] incorporates a segmentation head to estimate per-pixel degradation types, facilitating the model's adaptability to unseen degradations. By employing low-rank adapters, ABAIR efficiently integrates new degradation types with minimal parameter updates, enhancing its applicability in dynamic environments. Li *et al.* [193] proposed a U-shaped convolutional network designed to restore images degraded by various adverse weather conditions. It utilizes traditional 2D convolutions for feature extraction and incorporates a prompt generation module to create weather-specific prompts that guide the decoding process. Additionally, frequency separation via wavelet pooling is employed to enhance high-fidelity restoration.

B. Frequency and Feature Perturbation Techniques

Addressing the challenge of task interference in multi-degradation scenarios, AdaIR [194] leverages frequency mining and modulation to adaptively reconstruct images. By accentuating informative frequency subbands corresponding to specific degradations, AdaIR achieves state-of-the-art (SOTA) performance in tasks including denoising and de-hazing. Similarly, Degradation-aware Feature Perturbations (DFPIR) [195], employing channel-wise and attention-wise perturbations to align feature representations with the shared parameter space. This strategy mitigates task interference, enhancing the model's capability to handle multiple degradations such as noise and haze effectively.

TABLE I: Overview of image dehazing datasets: the first column lists key metadata (resolution, venue, best PSNR/SSIM), the second column describes the type of the dataset, while the third column describes dataset construction and insights.

RESIDE [154], TIP-19 Resolution: 620×460 36.39 / 0.988 [155]	Synthetic Dataset	**Subsets & Samples** ITS: 13.9k image pairs SOTS: 500 image pairs HSTs: 20 image pairs OTS: 72.1k image pairs RTTS: 4.3k image pairs Realistic Single Image Dehazing dataset (RESIDE). A large-scale synthetic training set, and two different sets designed for objective and subjective quality evaluations, respectively. This dataset includes both synthetic and real-world hazy images, divided into subsets like Indoor Training Set (ITS), Outdoor Training Set (OTS), Standard Testing Set (SOTS), Hybrid Subjective Testing Set (HSTS), and Real-world Task-driven Testing Set (RTTS). The synthetic images are generated using the atmospheric scattering model, combining clean images with depth information to simulate haze.
REVIDE [156], CVPR-21 Resolution: 2708×1800 25.79 / 0.899 [86]	Synthetic Dataset	**Samples: 48 video pairs.** A real-world video dehazing dataset for supervised learning, captured using a robot arm, Sony ICLE 6000 camera, and haze machines to ensure precise alignment of hazy and haze-free video pairs. It features indoor scenes with realistic atmospheric scattering, offering high-quality data for training and evaluating video dehazing models.
Dense-Haze [157], ICIP-19 Resolution: 5456×3632 17.55 / 0.67 [158]	Real Dataset	**Samples: 33 image pairs.** Real haze was produced using professional machines (LSM1500 PRO 1500 W) to mimic atmospheric conditions, with images captured under consistent lighting (cloudy, morning/evening) and low wind (<3 km/h) for uniform haze. Identical settings and static scenes ensured accurate haze-free and hazy image pairs.
NH-HAZE [159], CVPRW-20 Resolution: 1600×1200 29.46 / 0.890 [159]	Real Dataset	**Samples: 55 image pairs.** Non-Homogeneous Haze dataset. It is a real-world outdoor images, each consisting of a hazy image and its corresponding haze-free ground truth. To simulate realistic haze conditions, the authors employed a professional haze generator that produces non-uniform haze distributions, closely mimicking real atmospheric scenarios. Images were captured under consistent lighting and environmental settings to ensure accurate pairing between hazy and haze-free images.
BeDDE [160], ICME-19 Resolution: 1643×1200 0.9012/ 0.9725 (VI/RI) [161]	Real Dataset	**Samples: 208 image pairs.** This is the first real-world dataset of foggy images paired with aligned clear counterparts, captured across diverse outdoor scenes. Each pair includes manually labeled masks for region-specific evaluation. Two new metrics are introduced: Visibility Index (VI) for visibility enhancement and Realness Index (RI) for perceived naturalness—offering both objective and subjective assessment of defogging performance.
Night-Haze [162], DLCP-22 Resolution: 6000×4000 30.38/0.904 [163]	Real Dataset	**Samples: 32 image pairs, Extended: 64 image pairs.** All images were captured indoors to maintain consistent conditions, the dataset includes two scenes—one with simple geometric objects, the other with complex, detailed objects and localized lighting. Each scene was imaged under four lighting and four haze levels, yielding 16 images per scene (32 total). The extended version, Night-Haze-Ext, offers 64 images with additional haze levels, scene variations, and includes depth and thermal data.
HazeRD [164], ICIP-17 Resolution: ~3000×2448 18.55 / 0.85 [165]	Synthetic Dataset	**Samples: 14 image pairs.** The dataset contains 14 high-resolution (6–8 MP) haze-free RGB outdoor images, each paired with a depth map. Synthetic hazy versions are generated using the Koschmieder scattering model across five haze levels (visual ranges: 50m to 1000m), simulating varying atmospheric conditions based on scene geometry.
SOTS [154], TIP-19 Resolution: 620×460 39.42 / 0.996 [24]	Synthetic Dataset	**Samples: indoor 500 and 500 outdoor.** SOTS evaluates single-image dehazing under controlled settings with two subsets: SOTS-Indoor and SOTS-Outdoor, both containing synthetic hazy images. Haze-free images with estimated depth maps were used to generate realistic haze via the atmospheric scattering model.
DAVIS-2016 [153], CVIP-21 Resolution: 256×256 22.67 / 0.879 [86]	Synthetic Dataset	**Samples: 50 video pairs.** Synthetic Outdoor video de-hazing dataset that is generated synthetically and depth maps of each video frame of DAVIS-16 video dataset. Depth map of each respective frame in a video is estimated using the approach proposed in [166]. The attenuation coefficient = 2 and the atmospheric light value A = (0.8, 0.8, 0.8) were taken into account while generating the synthetic dataset.
NYU-Depth [167], ICCVW-11 Resolution: 256×256 23.81 / 0.897 [86]	Synthetic Dataset	**Samples: 45 video pairs.** Synthetic indoor dataset. It contains 45 videos divided into training (25 videos/ 28,222 frames) and testing (20 videos/ 7528 frames) videos. Depth maps are used to generate the synthetic hazy videos.
D-Hazy [168], IEEE CIP-16 Resolution: [640×480, 1024×768] 28.25 / 0.937 [169]	Synthetic Dataset	**Samples: 22 image pairs**. A high-quality synthetic image dataset is generated synthetically. Ground-truth clear images and depth maps were taken from the Middlebury stereo dataset. The Middlebury dataset provides high-quality stereo images along with accurate depth maps. These were used to simulate realistic haze conditions by varying parameters like Atmospheric light A, Scattering coefficient β.
I-Hazy [170], ACIVS-18 Resolution: 2833×4657 22.44 / 0.887 [24]	Synthetic Dataset	**Samples: 35 image pairs.** A total of 35 indoor scenes with varied household objects and surface properties were set up, each including a Macbeth ColorChecker for color calibration. For each scene, a haze-free image was captured under controlled lighting, followed by a hazy image after introducing real atmospheric-like haze using two fog machines (LSM1500 PRO 1500 W) and a fan to ensure even distribution. Both images were taken under identical lighting conditions.
V-Hazy [10], CVPR-20 Resolution: [640×480, 1024×768]	Synthetic Dataset	**Samples: 35 image pairs.** The author created a synthetic varicolored hazy image dataset by using the channel-wise spatial mean of real-world hazy images as atmospheric light, preserving the haze color. Hazy images were categorized into grayish, orange/yellow (smog), bluish, and other variants. Synthetic images were generated with haze densities defined by $\beta = 1, 3, 5$. Additionally, color-balanced versions were created using $A = (0.8, 0.8, 0.8)$ and the same β values.

C. State Space Models and Diffusion-Based Approaches

Models like DPMambaIR [196] combine a degradation-aware prompt state space model with a high-frequency enhancement block for fine-grained restoration of snow, haze, and noise. Diffusion-based methods [22], [197] use latent semantic mapping and conditional transformers to model weather-related distributions, but face challenges in generalizing to extreme or unseen conditions, with high computational costs and long inference times. AutoDIR [198] addresses these limitations using latent diffusion to adaptively restore diverse degradations, showing strong generalization for real-world scenarios.

D. Transformer-Based and Mixture-of-Experts Models

Transformer-based models like TransWeather [19] employ intra-patch attention and learnable weather-type embeddings within a unified encoder-decoder framework to adaptively restore images degraded by haze, snow, and other conditions. A vision transformer in [199] leverages contrastive learning to extract distortion-aware features for multi-weather restoration but shows performance drops when tested on unseen weather types. Adaptive sparse transformer in [185] leverages attentive feature refinement to mitigate noisy interactions for image restoration. The Weather-aware Multi-scale Mixture-of-Experts [200] dynamically routes inputs to specialized experts based on weather conditions, improving restoration under complex, mixed degradations such as snow and haze.

E. Architectural Search Approach

Li *et al.* [201] proposed a unified deep learning framework for multi-weather image restoration using neural architecture search (NAS), which automatically identifies optimal architectures for handling rain, snow, and haze, thereby improving generalization across diverse weather degradations.

F. Multi-Modality Approach

Siddiqua *et al.* [7] used a conditional GAN with multi-modal inputs *i.e.* RGB images and contextual information to restore the image. While effective, the model incurs high computational costs during both training and inference. A multi-domain attention-based conditional adversarial network is proposed in [202] for all-in-one image restoration.

G. Language-driven Approach

Ai *et al.* [12] introduces MPerceiver, a novel framework designed for comprehensive image restoration under diverse degradations. The proposed framework utilizes multimodal prompt learning, which combines textual and visual prompts

TABLE II: Overview of image deraining datasets: the first column lists key metadata (resolution, venue, best PSNR/SSIM), the second column describes the type of the dataset, while the third column describes dataset construction and insights.

RID [171], CVPR-19 Resolution: 512×512 7.625 / 7.492 / 23.93 / 34.61 [21]	Synthetic Dataset	**Samples: Indoor 16,200 and Outdoor 10,500.** The authors introduce NYU-Rain, a synthetic rain dataset built from NYU-Depthv2 images by rendering rain streaks and accumulation effects using depth information, including veiling and blur (see Algorithm 1). It comprises 16,200 samples, with 13,500 for training. They also create Outdoor-Rain, an outdoor rain dataset generated using depth estimated via state-of-the-art single-image depth methods, containing 9,000 training and 1,500 validation samples.
Rain12 [172], CVPR-16 Resolution: 512×512 36.69 / 0.962 [173]	Real Dataset	**Samples: 12 rainy images.** The authors proposed a realistic rain simulation model combining Rain Streaks (with varied shapes and directions) and Rain Accumulation (atmospheric veils mimicking mist/fog). A key innovation is the rain-streak binary map, labeling each pixel for streak presence to separate rain-affected areas from the background. The resulting dataset includes: (1) synthetic rainy images, (2) corresponding clean images, and (3) pixel-level binary maps of rain streaks.
RTTS [174], CVPR-19 Resolution: 620×460 24.76 / 42.04 [21]	Synthetic Dataset	**Samples: 13900 image pairs**. Realistic multi-purpose single image deraining dataset. Synthetic rain streak images created by overlaying computer-generated rain streaks onto clean images. Synthetic raindrop images generated by simulating raindrops on camera lenses, using a binary mask to define raindrop regions. Synthetic images that combine rain streaks with atmospheric scattering effects to simulate mist, using a model that includes transmission maps & atmospheric light.
RainCityscapes [175], CVPR-19 Resolution: 2048×1024 35.82 / 0.987 [176]	Synthetic Dataset	**Samples: ∼10,000 image pairs.** The RainCityscapes dataset was created by adding synthetic rain to Cityscapes images using a depth-guided, physically-inspired model. Rain streaks vary in length (based on speed and exposure), direction (wind-influenced), and transparency (more opaque at shallow depths). Depth maps enable realistic effects—closer objects show sharper streaks, while distant areas appear blurred. A veiling effect, simulating light scattering like fog, is added using depth-based exponential decay.
Rain800 [102], CVPR-19 Resolution: 512×512 32.00 / 0.923 [102]	Synthetic Dataset	**Samples: 800 image pairs.** The authors utilized clean images from publicly available datasets as the foundation for creating synthetic rainy images. Rain streaks were algorithmically added to the clean images to simulate various rain conditions. This process involved controlling parameters such as streak orientation, density, and intensity to mimic real-world rain patterns. Each synthetic rainy image was paired with its original clean counterpart.
Rain100H [177], CVPR-16 Resolution: 480×320 34.56 / 0.941 [178]	Synthetic Dataset	**Samples: 1900 image pairs.** This dataset contains high-quality synthetic rainy images with corresponding clean ground truth. Clean images from public datasets were used to generate diverse scenes, and rain was simulated using a Physical Rain Model and Layer-Based Separation. The rain model applied Gaussian-distributed streaks with varied length, width, and direction, along with motion blur to mimic real rain. The model assumes that the observed rainy image I is the sum of the background layer B and the rain streak layer R: $I = B + R$. This layered approach helped the network learn how to remove rain while preserving background details. Multiple rainy variants were created per clean image to simulate diverse conditions.
DID-Data [179], CVPR-17 Resolution: 512×512 35.66 / 0.967 [180]	Synthetic Dataset	**Samples: 13,200 image pairs.** Synthetic rainy images were created by adding artificially rendered rain streaks of varying intensity, direction, and appearance to high-quality clear images sourced online. Tools like Photoshop were used for realism. Each clean image was paired with multiple rainy variants, forming a supervised dataset of (rainy, clean) image pairs.
DIDMDN-Data [181], CVPR-18 Resolution: 512×512 30.57 / 0.8719 [182]	Synthetic Dataset	**Samples: 13,200.** Synthetic rainy images with light, medium, and heavy rain were created by adding simulated rain to clean images from datasets like BSD500 and UCID. Rain streaks of varying densities were generated with diverse orientations, sizes, and intensities, followed by motion blur for realism. These rain layers were blended with clean images, and each output was labeled by rain density. This enabled training a density-aware network using a large set of synthetic (rainy, clean) image pairs.
Real-world [183], CVPR-19 Resolution: 1000×1000 36.55 / 0.962 [184]	Real Dataset	**Samples: 29500 image pairs.** Spatially Aligned Paired Data is a large-scale real-world rainy image dataset captured using professional cameras. Each image pair—one with rain and one without—was taken from nearly identical viewpoints using tripods and remote shutters. Efforts were made to match illumination conditions, and frames with moving objects were manually selected to avoid mismatches. The resulting pairs have minimal misalignment, making them ideal for supervised learning.
R200H and R200L [101], CVPR-19 Resolution: 512×512 32.99 / 0.940 41.81 / 0.990 [180]	Synthetic Dataset	**Samples: 2000 image pairs.** Synthetic rainy images were generated by overlaying varied rain streaks (in angle, shape, transparency, and motion blur) onto clean outdoor backgrounds sourced from public datasets. Multiple rain layers simulated light and heavy rain. The rainy image formation followed $O = (B + R) \times T + A(1 - T)$, where O is the observed image, B the clean background, R rain streaks, T transmission, and A atmospheric light. Rain masks were also created to aid supervised training.
AGAN-Data [18], CVPR-18 Resolution: 512×512 32.45 / 0.937 [185]	Synthetic Dataset	**Samples: 1119 image pairs.** A synthetic dataset for raindrop removal was created using image pairs of identical scenes—one with raindrops and one clean—captured through two identical glass slabs (one sprayed with water). This setup avoids misalignment caused by refraction. Camera motion and environmental factors were controlled to ensure consistency. Images were captured using Sony A6000 and Canon EOS 60, with 3 mm thick glass placed 2–5 cm from the lens to vary raindrop patterns and minimize reflections.
ORD [186], IEEE SPL-13 Resolution: 96×96 32.05 / 0.952 [21]	Synthetic Dataset	**Samples: 9750 image (250,000 patches of size 96×96 pixels).** provided the degraded images with rain and fog having veiling effect degradation.

using stable diffusion priors to address various image degradations. Here, textual prompts used for holistic representations and visual prompts used for multi-scale detail refinement. Conde *et al.* [203] proposed an approach that uses real human-written instructions to solve multi-task image restoration. Yang *et al.* [204] introduces a language-driven all-in-one adverse weather removal approach that integrates natural language guidance into adverse weather restoration tasks. This language-driven method enhances flexibility and precision, enabling the system to handle diverse weather scenarios effectively. This approach demonstrates improved restoration quality and user-driven adaptability performance. The framework relies on pre-trained vision-language models to generate degradation priors. The dynamic selection of restoration experts through a Mixture-of-Experts (MOE) structure adds complexity to the model. This complexity may increase the difficulty of training and tuning the model effectively.

H. Knowledge Distillation Approach

Chen *et al.* [205] proposed a unified model for removing haze, snow, and rain using a single set of pretrained weights. It uses a two-stage knowledge learning process: Knowledge Collation transfers expertise from multiple teacher networks, while Knowledge Examination refines the student model with a multi-contrastive regularization loss. However, this framework introduces considerable training complexity and overhead.

I. Weather-General and Weather-Specific Approach

Zhu *et al.* [206] proposed a two-stage training strategy. In the first stage *i.e.,* Weather-General Feature Learning, the model learns general features common across different weather conditions by processing images with various weather-induced degradations to produce coarsely restored outputs. In the second stage *i.e.,* Weather-Specific Feature Learning, the model adaptively expands its parameters to capture specific characteristics unique to each weather type. This adaptive mechanism allows the model to handle distinct weather-related artifacts effectively. However, this method limits its scalability and adaptability in dynamic real-world environments where weather conditions can be highly variable.

J. Unknown Corruption Approach

Li *et al.* [207] proposed AirNet consisting of contrastive-based degraded encoder and degradation-guided restoration network. The first one aims to extract the latent degradation

TABLE III: Overview of image desnowing datasets: the first column lists key metadata (resolution, venue, best PSNR/SSIM), the second column describes the type of the dataset, while the third column describes dataset construction and insights.

SRRS [187], ECCV-20 Resolution: 1920×1080 32.39 / 0.98 [24]	Synthetic, Real Dataset	**Samples: Synthetic 50 video pairs (500 frames per video), Real-World: 5 videos (500 frames per video)** Captures video sequences of snowfall to reflect temporal snow dynamics—such as snowflake motion and veiling effects—not visible in static images. Clean videos were used to generate the dataset, with snow particles rendered using tools like Photoshop. Simulations vary in particle size, transparency, motion, and density (light to heavy). Real scenes are also included.
RVSD [121], ICCV-23 Resolution: 1920×1080 26.02 / 0.923 [188]	Synthetic Dataset	**Samples: 110 video pairs.** The authors created a comprehensive dataset for training and evaluating video snow removal algorithms using Unreal Engine 5 and augmentation techniques to simulate realistic snow and haze across diverse scenes and conditions.
Snow100K [189], TIP-18 Resolution: 640×640 33.92 / 0.96 [24]	Synthetic & Real set	**Samples: 100k synthesized snowy image pairs and 1,329 realistic snowy images.** To build a diverse snow image dataset, the authors synthetically added snow to clean images from sources like ImageNet and COCO, treating the originals as ground truth. Snowflakes—varying in size, shape, and transparency—were generated based on realistic distribution models and overlaid either randomly or in patterns. Each synthetic image includes a snow mask marking snowflake locations, enabling precise evaluation. Both opaque and translucent snow effects were simulated. Real snowy images were also collected (e.g., from Flickr), with manually annotated snow masks. The dataset is split into three subsets by snowflake size: Snow100K-S (small), Snow100K-M (small+medium), and Snow100K-L (small+medium+large), each with 33K images.
SnowCityScapes [190], TIP-21 Resolution: 512×256 38.60/0.9822 [122]	Synthetic Dataset	**Samples: 15,000 image pairs.** Based on the Cityscapes dataset, known for its high-quality urban street scenes. Utilized Adobe Photoshop to overlay synthetic snow onto the clean images. Encompasses three snow conditions: light, medium, and heavy snow. Comprises paired images: synthetic snowy images and their corresponding clean images. Maintains consistency with the original Cityscapes dataset in terms of image size and scene content.
SnowKITTI [190], TIP-21 Resolution: 1242×375 38.96 / 0.99 [133]	Synthetic Dataset	**Samples: 1,167 image pairs.** Derived from the KITTI 2012 dataset, which comprises real-world driving scenes. Utilized Adobe Photoshop to overlay synthetic snow onto the clean images. Simulated three snow conditions: light, medium, and heavy snow. It includes both training and testing sets. Each set contains image pairs: the synthetic snowy image and its corresponding clean image. Each image was augmented to simulate 3 snow conditions: light, medium, and heavy snow.
CSD [123], TCSVT-21 Resolution: 640×480 32.95 / 0.942 [21]	Synthetic Dataset	**Samples: 110 pairs of videos.** CSD combines synthetic and real snowy images for training and evaluation. Snow-free backgrounds from datasets like ImageNet and COCO were overlaid with simulated snowflakes of varying size, shape, opacity, and motion blur using layered alpha blending to create light, medium, and heavy snowfalls. Real-world snowy images were also sourced from platforms like Flickr and Google, selected for clear snowfall and diverse conditions.

representation. Second restores the clean image from the input with unknown degradation.

V. Datasets for Image and Video Restoration

In this Section, we have discussed the benchmark image and video datasets utilized to compare the current SOTA approaches for image/video de-hazing, de-raining and de-snowing tasks. The datasets are broadly classified into synthetic and real-world datasets. The TABLE I, II and III provides a detailed overview of benchmark datasets used for respective application. Each row corresponds to a specific dataset, the first column includes metadata such as spatial resolution, publication venue, and best reported PSNR/SSIM values, while second column describes the dataset type (synthetic or real), and third column gives the insights into the construction methodology of each dataset, such as whether the images were synthetically generated, collected from real-world scenes, or created using paired or unpaired data. This structured comparison highlights the diversity in dataset design and evaluation standards across different weather degradation types, underlining the importance of high-quality, realistic datasets for the effective benchmarking and development of robust restoration algorithms.

VI. Loss Functions

Here, we have discussed the various existing loss-functions. Table IV presents a comprehensive summary of various loss functions commonly employed in image/video restoration tasks such as de-hazing, de-raining, and de-snowing. The first column lists the names of the loss functions, the second column provides their corresponding mathematical formulations, and the third column offers descriptions of their roles and applications in restoration models. These loss functions ranging from basic pixel-wise losses like L1 and L2 to more advanced perceptual, adversarial, and structural losses. These losses are crucial in guiding models to produce visually and quantitatively improved results. The descriptions highlight how each loss function contributes differently to model performance, such as improving edge sharpness, preserving texture details, or enhancing perceptual similarity. This structured presentation aids in understanding the trade-offs and suitability of loss functions for types of weather degradation scenarios.

VII. Experimental Results and Discussion

We have evaluated and compared current SOTA approaches in terms of quantitative and qualitative results. PSNR and SSIM estimates have been employed to reference-based evaluation analysis. While, NIQE, Entropy, BRISQUE and PIQE are used for non-reference evaluation analysis. Detailed description of the reference and no-reference evaluation metrics are summarized in Table V.

A. Quantitative Analysis

The non-reference evaluation analysis for de-hazing, and de-raining on RTTS [174], and RID [171] datasets is provided in TABLE VI respectively. The Average NIQE (↓), Entropy (↑), BRISQUE (↓) and PIQE (↓) are considered as non-reference parameters (*↓ represent lower is better, ˆ represent higher is better*). For this analysis, the recent unified multi-weather restoration approaches such as UMVR [1], KD [20], TW [19], Diffusion [22], WGWS [206] and DTMIR [21] are considered.

Furthermore, the reference-based parameter analysis in terms of average PSNR and SSIM is presented in TABLE VII to TABLE XV across benchmark datasets for various restoration tasks and three types of methods/models are compared: single-task methods (specialized for a specific degradation such as haze, rain, or snow), multi-task/multi-weather models (task-wise fine-tuned and evaluated across multiple tasks), and all-in-one restoration models (trained once on a combined dataset to handle diverse degradations including blur, noise, low-light, and adverse weather in a unified framework). In TABLE VII to TABLE XIV, the first, second, and third partitions respectively correspond to single-task, multi-task/multi-weather, and all-in-one approaches.

B. Qualitative Analysis

In this section, the visual result analysis on day and night-time degraded images is provided. Refer Figure 4 for day-time

TABLE IV: Commonly used loss functions in image/video restoration tasks such as dehazing, deraining, and desnowing.

Loss Function	Mathematical Equation	Description and Usage
Image Similarity Loss (PSNR-based)	$L_{\text{psnr}} = \frac{10}{\log_{10}} \cdot \frac{1}{B} \sum_{b=0}^{B-1} \log(\lVert I_{\text{rst}} - I_{\text{gt}} \rVert_2 + \epsilon)$	Measures pixel-wise quality via log-MSE; higher PSNR reflects better perceptual similarity and aids in tracking restoration tasks training.
Weather Classification Loss	$L_{\text{cls}} = -\frac{1}{B} \sum_{b=1}^{B} \sum_{c=1}^{M} y_{bc} \log(p_{bc})$ $y_{bc} \in \{0, 1\}$: indicator if class c is the true label for sample b	A cross-entropy loss applied for classifying weather types (e.g., haze, rain, snow). Enables multi-task learning in restoration networks where weather condition labels assist in accurate image enhancement.
Reconstruction and Restoration Losses	$L_{\text{rec}} = \lVert X' - X \rVert_1, \quad L_{\text{res}} = \lVert Y' - Y \rVert_1,$ $L_{\text{acc}} = \lVert \text{Model}(Y' - X) - Y \rVert_1$	X: degraded image, Y: ground truth, X', Y': reconstructed outputs. These losses ensure fidelity at both representation and output level. Commonly used in encoder-decoder setups to guide accurate reconstruction.
Charbonnier Loss	$L_{\text{char}} = \sqrt{\lVert I^c - \hat{I} \rVert^2 + \varepsilon^2}, \quad \varepsilon = 10^{-4}$	A smooth, robust variant of L2 loss, commonly used in image restoration for preserving sharp details and ensuring training stability.
Edge Loss	$L_{\text{edge}} = \sqrt{\lVert \nabla I^c - \nabla \hat{I} \rVert^2 + \varepsilon^2}$	Encourages edge consistency using image gradients (Laplacian/Sobel), aiding fine-detail and texture restoration.
Mean Squared Error (MSE)	$\mathcal{L}_{\text{MSE}} = \frac{1}{N} \sum_{i=1}^{N} (x_i - \hat{x}_i)^2$	Penalizes squared pixel differences; standard for regression. Enables smooth restoration but can cause blurriness when used alone.
L1 Loss (MAE)	$\mathcal{L}_{\text{L1}} = \frac{1}{N} \sum_{i=1}^{N} \lvert x_i - \hat{x}_i \rvert$	Less sensitive to outliers than MSE, L1 loss preserves edges and yields sharper outputs by promoting pixel-wise sparsity. Commonly used in image restoration.

TABLE V: Common reference and no-reference evaluation metrics for image/video quality and generative model assessment.

Metric	Mathematical equation	Description and usage
SSIM	$\text{SSIM}(x, y) = \frac{(2\mu_x\mu_y + C_1)(2\sigma_{xy} + C_2)}{(\mu_x^2 + \mu_y^2 + C_1)(\sigma_x^2 + \sigma_y^2 + C_2)}$	Measures structural similarity between two images by combining luminance, contrast, and structural comparisons. Value ranges from -1 to 1, with 1 indicating perfect similarity.
PSNR	$\text{PSNR} = 10 \cdot \log_{10}\left(\frac{\text{MAX}^2}{\text{MSE}}\right)$	Measures the ratio of peak signal to noise power; higher PSNR indicates better quality.
LPIPS	— (No closed-form; computed using pretrained deep networks)	Measures perceptual similarity via deep features; lower LPIPS implies better similarity. Widely used in generative models.
FID	$\text{FID} = \lVert \mu_r - \mu_g \rVert^2 + \text{Tr}\left(\Sigma_r + \Sigma_g - 2(\Sigma_r\Sigma_g)^{1/2}\right)$	Compares real vs. generated features using InceptionNet; lower scores imply better generation. Sensitive to mode collapse.
NIQE	$\text{NIQE}(x) = (\mu_x - \mu_n)^T (\Sigma_x + \Sigma_n)^{-1} (\mu_x - \mu_n)$	Quantifies naturalness by comparing image features to natural scene stats; lower NIQE scores indicate better perceptual quality.
BRISQUE	— (Model trained on NSS features and SVM regression)	Extracts spatial scene statistics & uses an SVM trained on subjective scores to predict quality. Low score better quality.
Entropy	$H(I) = -\sum_{i=0}^{255} p(i) \log_2 p(i)$	Measures image texture complexity; higher entropy may indicate more detail but doesn't always reflect perceptual quality.
PIQ	— (Deep feature-based metric, no analytical formula)	Estimates perceptual quality using deep features & learned weights, combining cues like sharpness, contrast, and texture. Lower scores indicate better quality.

and night-time analysis. The UMVR [1], KD [20], TW [19], Diffusion [22], WGWS [206] and DTMIR [21] methods are considered for visual result analysis purpose.
Result analysis for day-time degradations:

- **De-hazing analysis**: Every approach producing significant results (*row 1 and 7 from Figure 4*) with some limitations like lacks sharpness in distant details (UMVR [1]), artifacts near edges and reduces visual consistency (KD [20]), color distortions (TW [19]), tends to smooth textures (Diffusion [22]), over-enhance edges (DTMIR [21]).
- **De-raining analysis**: The de-raining results (*row 2 and 8 from Figure 4*) achieved by existing methods are significant. However, each methods having it's own limitations like background smoothing (UMVR [1]), some streaks and artifacts remain in regions with high rain density (KD [20]), losing texture details (TW [19]), color tones appear slightly unnatural (Diffusion [22]).
- **De-snowing analysis**: The existing methods achieved significant performance for snow removal task (*row 3 and 6 from Figure 4*). However, limitations like over-smooth regions ((KD) [20]), unnatural smoothing in darker regions (Diffusion [22]), over-saturation (DTMIR [21]), larger snow regions are still need to handle effectively.

The methods UMVR [1], KD [20], TW [19], Diffusion [22], WGWS [206] and DTMIR [21] are trained on day-time hazy, rainy and snowy degradations. These models are directly tested on night-time degraded images and results are provided in Figure 4. From the results, it is clear that the existing SOTA methods are able to handle night-time degradations to some extent. Detailed analysis for night-time degradations is:

- **De-hazing analysis**: The results (refer row 4 and 10 from Figure 4) are reasonable for night-time haze removal task. There are various limitations like haze remains in distant areas (UMVR [1]), brighter regions reduces naturalness (KD [20]), uneven haze removal (TW [19]), introducing

TABLE VI: Subjective result Analysis on Real-world De-hazing (RTTS [154]), De-raining with Veil (RID [171]) & in terms of Average NIQE, Entropy (ENT), Brisque (BRQ) & PIQE (PIQ).

	Method	Parameter	UMVR [1] (TMM-22)	KD [20] (CVPR-22)	TransWeather [19] (CVPR-22)	Diffusion [22] (TPAMI-23)	WGWS [206] (CVPR-23)	DTMIR [21] (ICCV-23)
Dataset	RTTS	NIQE (↓)	5.009	4.996	5.703	5.315	6.199	**4.859**
		ENT (↑)	7.221	7.297	7.263	7.115	7.064	**7.505**
		BRQ (↓)	28.625	26.837	29.874	29.897	35.715	**24.761**
		PIQ (↓)	42.749	45.561	43.784	50.386	55.296	**42.037**
	RID	NIQE (↓)	**6.604**	6.943	7.496	7.103	6.813	7.625
		ENT (↑)	7.486	7.459	7.393	7.401	7.348	**7.492**
		BRQ (↓)	24.296	24.841	24.165	24.021	24.862	**23.931**
		PIQ (↓)	**33.289**	38.398	39.141	36.651	35.094	34.614

TABLE VII: Quantitative analysis of raindrop removal on AGAN-Data [18]

Method	PSNR	SSIM
Eigen's [208]	21.31	0.757
Pix2pix [209]	27.20	0.836
CCN [210]	31.34	0.929
Quan's [211]	31.37	0.918
AttenGAN [18]	31.59	0.917
IDT [106]	31.87	0.931
Uformer [145]	29.42	0.906
TKLMR [205]	30.99	0.927
DuRN [212]	31.24	0.926
MAXIM-2S [213]	31.87	0.935
All-in-One [201]	31.12	0.927
Diffusion128 [22]	29.66	0.923
TransWeather [19]	30.17	0.916
Diffusion64 [22]	30.71	0.931
AWRCP [214]	31.93	0.931
AST-B [185]	**32.45**	**0.937**

TABLE VIII: Single task evaluation: Video dehazing comparison on REVIDE dataset [156]

Method	PSNR	SSIM
DCP [28]	11.03	0.728
STMRF [215]	15.54	0.693
FDVD [216]	16.37	0.656
GDN [217]	19.69	0.854
EVDNET [218]	17.41	0.808
MSBDN [219]	22.01	0.876
FFA [155]	16.65	0.813
VDN [220]	16.64	0.813
RDNet [221]	16.93	0.804
DAID [222]	19.20	0.821
EDVR [223]	21.22	0.874
PDVD [224]	22.69	0.875
CG-IDN [156]	23.21	0.884
LRNET [84]	23.89	0.896
DSTM [153]	25.53	0.894
DRFNET [85]	25.74	0.898
CRFNet [86]	**25.79**	**0.899**

TABLE IX: Single task evaluation: Dehazing comparison on DAVIS-2016 and NYU Depth.

Method	DAVIS-2016		NYU Depth	
	PSNR	SSIM	PSNR	SSIM
TCN [225]	16.61	0.619	18.83	0.614
FFA [155]	14.19	0.650	17.74	0.715
MSBDN [219]	15.41	0.706	16.67	0.658
GCANet [140]	20.31	0.728	16.93	0.650
RRO [226]	15.09	0.760	19.47	0.842
FMENet [227]	16.16	0.830	19.81	0.843
CANCB [228]	16.44	0.834	20.87	0.890
RDNet [221]	19.38	0.788	14.85	0.561
DAID [222]	16.71	0.776	22.63	0.876
DSTM [153]	21.71	0.877	23.26	0.865
DRFNET [85]	22.62	0.879	23.64	0.874
LRNET [84]	22.04	0.835	**24.87**	**0.919**
CRFNet [86]	**22.67**	**0.880**	23.81	0.897

TABLE X: Comparative quantitative result analysis of SOTA approaches for Dense-Haze [229] for real haze removal.

Method	Dense-Haze	
	PSNR	SSIM
RIDCP [230]	8.09	0.42
DCP [28]	10.06	0.39
SGID [45]	13.09	0.52
D4 [67]	13.12	0.53
AOD-Net [231]	13.14	0.41
GridDehazeNet [41]	13.31	0.37
DA-Dehaze [222]	13.98	0.37
FFA [155]	14.39	0.45
AECR-Net [66]	15.80	0.47
DFormer [56]	16.29	0.51
DeHamer [232]	16.62	0.56
MBTFormer-B [233]	16.66	0.56
Uformer [145]	15.22	0.43
Restormer [144]	15.78	0.55
Fourmer [146]	15.95	0.49
ResFlow [150]	17.12	0.59
AST-B [185]	17.27	0.57
Defusion [158]	**17.55**	**0.67**

TABLE XI: Comparative quantitative result analysis of SOTA approaches for SPAD [183] for rain streak removal.

Method	SPAD	
	PSNR	SSIM
DDN [179]	36.16	0.9463
RESCAN [98]	38.11	0.9797
PReNet [173]	40.16	0.9816
RCDNet [234]	43.36	0.9831
SPDNet [235]	43.55	0.9875
DualGCN [236]	44.18	0.9902
SEIDNet [237]	44.96	0.9911
Fu et al. [238]	45.03	0.9907
SCD-Former [239]	46.89	0.9941
IDT [106]	47.34	0.9929
SPAIR [240]	44.10	0.9872
Restormer [144]	46.25	0.9911
MPRNet [142]	45.00	0.9897
Uformer [145]	47.84	0.9925
DRSformer [241]	48.53	0.9924
AST-B [185]	**49.72**	**0.9944**

TABLE XII: Reference Parameter Analysis for De-hazing with Rain+haze, De-raining with RainDrop and Snow with SNOW 100K Datasets in terms of Average PSNR/SSIM.

Method	RTTS [171]		AGAN Data [18]		SNOW 100K [189]	
	PSNR	SSIM	PSNR	SSIM	PSNR	SSIM
AOD-Net [231] (ICCV-17)	24.71	0.898	31.12	0.927	28.33	0.882
Restormer [144] (CVPR-22)	27.24	0.920	29.29	0.937	27.76	0.906
MPRNet [142] (CVPR-21)	28.08	0.931	29.45	0.941	27.92	0.911
Uformer [145] (CVPR-23)	25.40	0.889	27.38	0.919	26.60	0.887
LPM [242] (TIP-24)	28.68	0.940	30.40	0.956	28.54	0.922
ResFlow [150] (CVPR-25)	-	-	32.82	0.936	31.86	0.917
TW [19] (CVPR-22)	28.83	0.900	30.17	0.916	29.31	0.888
KD [20] (CVPR-22)	24.20	0.904	30.47	0.954	26.96	0.897
WeaFU [197] (TCSVT-24)	-	-	-	-	29.49	0.920
MWFormer [199] (TIP-24)	30.27	0.912	31.91	0.927	30.92	0.909
Diffusion [22] (TPAMI-23)	29.64	0.931	30.71	**0.931**	30.09	0.904
MWCNet [193] (TCSVT-25)	**30.78**	**0.949**	31.18	0.940	30.92	0.923
Defusion [158] (CVPR-25)	-	-	**33.81**	**0.967**	**32.11**	**0.926**

minor artifacts in darker regions (Diffusion [22]) need to handle effectively.

- **De-raining analysis**: For night-time rain-removal task, the existing methods achieved significant performance (row 5 and 11 from Figure 4). However, these methods are suffering from different artifacts, loosing finer details, over-enhancement, handling heavy rain, etc.
- **De-snowing analysis**: The provided results (row 9 and 12 from Figure 4) shows satisfactory performance for night-time snow removal task. But, issues such as over-smoothing, excessive blurring, and reduced texture clarity should be effectively handled.

C. Computational Complexity Analysis

Any image or video restoration method act as a pre-processing step for high vision tasks like object detection, activity recognition [253], [254], etc. Therefore, maintaining effective computational complexity is important aspect for real-world applications. The TABLE XVI shows the computational complexity analysis of the existing multi-weather methods in terms of number of trainable parameters, size and

TABLE XIII: Comparative quantitative result analysis of SOTA approaches for snow removal.

Method	Snow 100K [189]		SRRS [187]		CSD [123]	
	PSNR	SSIM	PSNR	SSIM	PSNR	SSIM
MGF [243]	22.41	0.77	15.78	0.74	13.98	0.67
DesnowNet [189]	30.11	0.93	20.38	0.84	20.13	0.81
S-Attention [211]	29.94	0.89	26.56	0.90	27.85	0.88
JSTASR [244]	28.59	0.86	25.82	0.89	27.96	0.88
DesnowGAN [130]	31.11	0.95	-	-	27.09	0.88
InvDN [245]	27.99	0.81	26.49	0.88	27.46	0.86
HDCW-Net [123]	24.10	0.80	27.78	0.92	29.06	0.91
InvDSNet [134]	32.41	0.93	29.25	0.95	31.85	0.96
CCN [246]	**33.64**	**0.95**	**37.15**	**0.99**	**32.70**	**0.98**
ResFlow [150]	31.86	0.917	-	-	-	-
TransWeathe [19]	32.06	0.94	29.05	0.95	31.13	0.95
Defusion [158]	32.11	0.926	-	-	-	-

TABLE XIV: Reference Parameter Analysis for De-hazing with SOTS, De-raining with ORD and Snow with CSD Datasets in terms of Average PSNR/SSIM.

Method	SOTS [154]		CSD [123]		ORD [186]	
	PSNR	SSIM	PSNR	SSIM	PSNR	SSIM
UMVR [1] (TMM-22)	33.41	0.980	28.65	0.900	22.99	0.830
DTMIR [21] (ICCV-23)	**36.26**	**0.987**	**32.95**	**0.942**	**31.24**	**0.951**
KD [20] (CVPR-22)	34.64	0.985	31.35	0.950	29.05	0.916
TransWeather [19] (CVPR-22)	32.45	0.955	29.76	0.940	27.96	0.950

GFLOPs. The number of trainable parameters, size of the DTMIR [21] is 11M and 44.01MB respectively which is less than all other methods. The GFLOPs of TW [19] is 12.24G which is less than all other methods.

VIII. Research Needs and Future Directions

A. Research Needs

- **Comprehensive Benchmark Datasets:** There remains a critical need for large-scale, high-resolution datasets encompassing diverse weather conditions—such as rain, snow, haze, fog, and dust—captured under varying intensities and geographic contexts. Such datasets should include both image and video sequences with temporally consistent annotations to support training and evaluation of robust models across daytime and nighttime scenarios in transportation environments.
- **Generalized Multi-weather Restoration Models:** While several recent approaches demonstrate the ability to handle multiple weather degradations, their generalization to unseen or compound conditions remains limited. Enhancing the scalability and robustness of such models—particularly under dynamic and mixed weather scenarios—requires improved architectures trained on diverse, representative datasets.
- **Real-time and Edge-Efficient Processing:** For deployment in smart transportation systems, restoration models must operate in real-time on resource-constrained edge devices, such as those used in ADAS or autonomous vehicles. Research should focus on lightweight model architectures and optimization strategies, including quantization, pruning, knowledge distillation, and neural architecture search (NAS), to achieve the balance between speed, energy efficiency, and accuracy.

TABLE XV: Comparisons under All-in-one restoration setting: single model trained on a combined set of images originating from different degradation types. When averaged across different tasks, PromptIR provides a significant gain of 0.86 dB over the previous all-in-one method AirNet [207] in terms of PSNR/SSIM.

Method	**Dehazing** SOTS [154]	**Deraining** Rain100L [177]	**Denoising on BSD68 dataset** $\sigma = 25$	$\sigma = 50$
BRDNet [247] (NN-20)	23.23/0.895	27.42/0.895	29.76/0.836	26.34/0.836
LPNet [248] (CVPR-19)	20.84/0.828	24.88/0.784	24.77/0.748	21.26/0.552
FDGAN [249] (CVPR-20)	24.71/0.924	29.89/0.933	28.81/0.868	26.43/0.776
MPRNet [142] (CVPR-21)	25.28/0.954	33.57/0.954	30.89/0.880	27.56/0.779
DL [250] (TPAMI-21)	26.92/0.391	32.62/0.931	30.41/0.861	26.90/0.740
AirNet [207] (CVPR-22)	27.94/0.962	34.90/0.967	31.26/0.888	28.00/0.797
PromptIR [191] (ANIPS-23)	30.58/0.974	36.37/0.972	31.31/0.888	28.06/0.799
AdaIR [194] (arXiv-24)	31.06/0.980	38.64/0.983	31.45/0.892	28.19/0.802
MoCE-IR [251] (CVPR-25)	31.34/0.979	38.57/**0.984**	31.45/0.888	28.18/0.800
InstructIR [203] (ECCV-24)	30.22/0.959	37.98/0.978	**31.52**/0.890	**28.30**/0.804
DFPIR [195] (CVPR-25)	**31.87/0.980**	**38.65**/0.982	31.47/**0.893**	28.25/**0.806**

TABLE XVI: Computational Complexity analysis of SOTA Methods in Terms of Number of Trainable Parameters, FLOPs and Inference Time (sec/frame).

Methods	Parameters	Size(MB)	GFLOPS
LPM [242] (TIP-24)	126M	1700	51.5
MPRNet [142] (CVPR-21)	16M	3600	6534
KD [20] (CVPR-22)	28M	348.89	49.22
Diffusion [22] (TPAMI-23)	110M	1296.71	475.43
WGWS [206] (CVPR-23)	5.97M	-	-
Uformer [145] (CVPR-23)	51M	2900	357.8
MoCE-IR [251] (CVPR-25)	11.47M	-	39.25
ACL [252] (CVPR-25)	4.6M	-	55
TransWeather [19] (CVPR-22)	31M	148.77	**12.24**
DTMIR [21] (ICCV-23)	11M	**44.01**	67.44
UMVR [1] (TMM-22)	**0.31M**	-	-

- **Domain Adaptation and Synthetic-to-Real Generalization:** Models trained on synthetic weather often underperform in real-world settings. Bridging this gap requires domain adaptation and self-supervised learning. Techniques like unsupervised adaptation, style transfer, and GAN-based learning support robust transfer to real-world driving scenarios.

B. Future Directions

- **Multi-weather Video Restoration Approaches:** Limited video based multi-weather restoration approaches [153], [152] are proposed. Real-time video restoration is essential for ADAS and autonomous vehicles to ensure vehicle and pedestrian safety.
- **All-Weather-Robust Downstream Tasks:** Current state-of-the-art multi-weather image restoration approaches provide significant results on limited tasks. As restoration is a pre-processing task, there is a need to perform main computer vision tasks like object detection, depth estimation [255], [256], activity recognition [257], etc. for high level applications. Recent works [258], [259] have proposed restoration followed by the object detection task in single algorithm. However, they consider only five categories (Person, Bicycle, Car, Motorbike and Bus) of object detection. This can be extended to further categories of object detection. Similarly, the models of

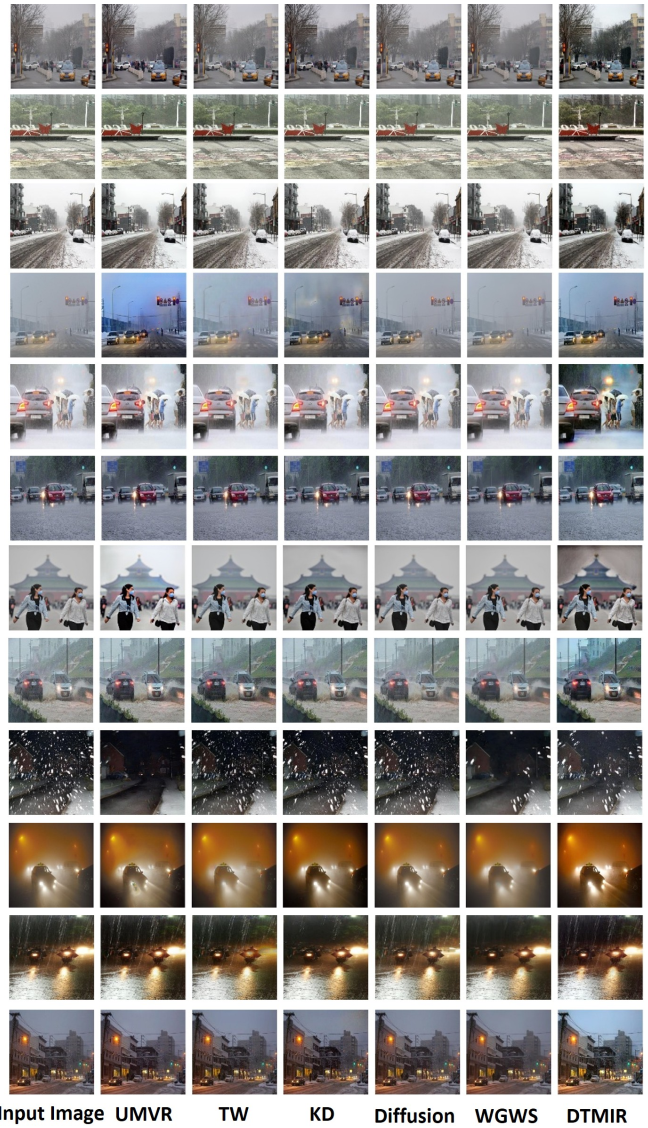

Figure 4: Visual result analysis of the existing methods: UMVR [1] (TMM-22), KD [20] (CVPR-22), TW [19] (CVPR-22), Diffusion [22] (TPAMI-23), WGWS [206] (CVPR-23) and DTMIR [21] (ICCV-23) on complex situations of real-world weather degraded image restoration.

activity recognition, depth estimation [260] and other main computer vision tasks can also be proposed without performing restoration task for degraded images/videos.

- **Weather-Adaptive Neural Networks:** Developing neural architectures that adapt dynamically to varying weather conditions is a promising direction. Self-attention mechanisms, weather classifiers, and reinforcement learning can guide adaptive behavior, enabling models to prioritize specific degradations and optimize restoration performance in real-time.
- **Energy-efficient Implementations:** Design of lightweight multi-weather restoration models is the need for deployment in embedded and automotive systems. To develop lightweight model without significant performance loss some techniques can be helpful, like weight sharing, pruning, tensor decomposition, and binary/ternary quantization.
- **Restoration Under Mixed and Compound Degradations:** In real-world transportation scenarios, visual data often suffers from multiple simultaneous degradations—such as haze combined with rain and noise, or blur co-occurring with fog and snow. While most existing models are tailored to handle individual weather effects, their performance typically deteriorates under such complex conditions. Recently, an emerging direction [261] has explored the use of agentic AI pipelines to tackle compound degradations by decomposing the problem into modular tasks and dynamically coordinating specialized restoration agents. This paradigm shows strong potential for scalable and generalizable restoration in real-world applications. Future research can build on these early efforts by further enhancing task decomposition, inter-agent communication, and real-time adaptability for dynamic, multi-degradation scenarios.

IX. Conclusion

The significant challenges posed due to adverse weather conditions for various applications like autonomous driving, surveillance, and remote sensing are discussed. Further, the development of weather specific and multi-weather restoration approaches with specific limitations from traditional to learning (CNNs, GANs, Transformer, Diffusion, Knowledge distillation and Multimodal) based techniques are discussed. Recent advancements with learning techniques have demonstrated superior performance by capturing complex features. However, challenges related to more diverse datasets, limited video-based multi-weather restoration, all weather object detection with diverse categories still need to be addressed. This survey aims to guide future research efforts, encouraging innovation in multi-weather video restoration and all-weather object recognition to enhance visibility and safety across diverse domains.

References

[1] A. Kulkarni, P. W. Patil, S. Murala, and S. Gupta, "Unified multi-weather visibility restoration," *IEEE Transactions on Multimedia*, vol. 25, pp. 7686–7698, 2022.

[2] R. Zhu, M. Wu, X. Xiong, X. Zhu, and Y. Fan, "Multi-weather degradation-aware transformer for image restoration," in *IEEE ICASSP*. IEEE, 2024, pp. 3765–3769.

[3] A. Gautam, A. Pawar, A. Joshi, S. N. Tazi, S. Chaudhary, P. Hambarde, A. Dudhane, S. Vipparthi, and S. Murala, "Pureformer: Transformer-based image denoising," in *Proceedings of the Computer Vision and Pattern Recognition Conference*, 2025, pp. 1441–1449.

[4] Y. Dai, C. Li, S. Zhou, R. Feng, Q. Zhu, Q. Sun, W. Sun, C. C. Loy, J. Gu, S. Liu *et al.*, "Mipi 2023 challenge on nighttime flare removal: Methods and results," in *Proceedings of the IEEE/CVF conference on computer vision and pattern recognition*, 2023, pp. 2853–2863.

[5] P. Alaspure, P. Hambarde, A. Dudhane, and S. Murala, "Darkgan: night image enhancement using generative adversarial networks," in *International Conference on Computer Vision and Image Processing*. Springer, 2020, pp. 293–302.

[6] L.-W. Kang, K.-L. Chou, and R.-H. Fu, "Deep learning-based weather image recognition," in *International Symposium on Computer, Consumer and Control (IS3C)*. IEEE, 2018, pp. 384–387.

[7] M. Siddiqua, N. Akhter, and J. Khurshid, "Multi-modal visibility improvement under abnormal weather conditions using contextual conditional gan," in *International Conference on Emerging Technologies (ICET)*. IEEE, 2021, pp. 1–6.

[8] P. W. Patil, S. Gupta, S. Rana, and S. Venkatesh, "Video restoration framework and its meta-adaptations to data-poor conditions," in *ECCV*, 2022, pp. 185–200.

[9] A. Kulkarni and S. Murala, "Wipernet: A lightweight multi-weather restoration network for enhanced surveillance," *IEEE Transactions on ITS*, vol. 23, no. 12, pp. 24 488–24 498, 2022.

[10] A. Dudhane, K. M. Biradar, P. W. Patil, P. Hambarde, and S. Murala, "Varicolored image de-hazing," in *CVPR*, 2020, pp. 4564–4573.

[11] V. Musat, I. Fursa, and P. Newman, "Multi-weather city: Adverse weather stacking for autonomous driving," in *ICCV Workshop*, 2021, pp. 372–381.

[12] Y. Ai, H. Huang, X. Zhou, J. Wang, and R. He, "Multimodal prompt perceiver: Empower adaptiveness generalizability and fidelity for all-in-one image restoration," in *CVPR*, 2024, pp. 25 432–25 444.

[13] Y. Wang, S. Liu, C. Chen, and B. Zeng, "A hierarchical approach for rain or snow removing in a single color image," *IEEE TIP*, vol. 26, no. 8, pp. 3936–3950, 2017.

[14] M. Zandersen, J. S. Oddershede, and A. B. Pedersen, "Nature based solutions for climate adaptation-paying farmers for flood control," *Ecological Economics*, vol. 181, p. 106919, 2021.

[15] X. Zhang, T. Wang, W. Luo, and P. Huang, "Multi-level fusion and attention-guided cnn for image dehazing," *IEEE Transactions on CSVT*, vol. 31, no. 11, pp. 4162–4173, 2020.

[16] W. Fan, M. Weixin, W. Le, D. Peng, and L. Junbo, "A semi-supervised video dehazing method based on cnns," *Research Square*, pp. 6391–6403, 2024.

[17] W. Wan and H. J. Lee, "Perceptual generative adversarial network for single image de-snowing," *KIPS Transactions on Software and Data Engineering*, vol. 8, no. 10, pp. 403–410, 2019.

[18] R. Qian, R. T. Tan, W. Yang, J. Su, and J. Liu, "Attentive generative adversarial network for raindrop removal from a single image," in *CVPR*, 2018, pp. 2482–2491.

[19] J. M. J. Valanarasu, R. Yasarla, and V. M. Patel, "Transweather: Transformer-based restoration of images degraded by adverse weather conditions," in *CVPR*, 2022, pp. 2353–2363.

[20] W.-T. Chen, Z.-K. Huang, C.-C. Tsai, H.-H. Yang, J.-J. Ding, and S.-Y. Kuo, "Learning multiple adverse weather removal via two-stage knowledge learning and multi-contrastive regularization: Toward a unified model," in *2022 IEEE/CVF Conference on CVPR*, 2022, pp. 17 632–17 641.

[21] P. W. Patil, S. Gupta, S. Rana, S. Venkatesh, and S. Murala, "Multi-weather image restoration via domain translation," in *ICCV*, 2023, pp. 21 696–21 705.

[22] O. Özdenizci and R. Legenstein, "Restoring vision in adverse weather conditions with patch-based denoising diffusion models," *IEEE TPAMI*, vol. 45, no. 8, pp. 10 346–10 357, 2023.

[23] R. Kumar, R. Balasubramanian, and B. K. Kaushik, "Efficient method and architecture for real-time video defogging," *IEEE Transactions on ITS*, vol. 22, no. 10, pp. 6536–6546, 2020.

[24] Y. Cui, W. Ren, X. Cao, and A. Knoll, "Revitalizing convolutional network for image restoration," *IEEE TPAMI*, vol. 46, no. 12, pp. 9423–9438, 2024.

[25] A. Dudhane, O. Thawakar, S. W. Zamir, S. Khan, F. S. Khan, and M.-H. Yang, "Dynamic pre-training: Towards efficient and scalable all-in-one image restoration," *arXiv preprint arXiv:2404.02154*, 2024.

[26] A. Dudhane, S. W. Zamir, S. Khan, F. S. Khan, and M.-H. Yang, "Burst image restoration and enhancement," in *Proceedings of the ieee/cvf Conference on Computer Vision and Pattern Recognition*, 2022, pp. 5759–5768.

[27] P. Patil, J. Singh, P. Hambarde, A. Kulkarni, S. Chaudhary, and S. Murala, "Robust unseen video understanding for various surveillance environments," in *18th IEEE International Conference on Advanced Video and Signal Based Surveillance (AVSS)*. IEEE, 2022, pp. 1–8.

[28] K. He, J. Sun, and X. Tang, "Single image haze removal using dark channel prior," *IEEE TPAMI*, vol. 33, no. 12, pp. 2341–2353, 2011.

[29] J. Wang, N. He, L. Zhang, and K. Lu, "Single image dehazing with a physical model and dark channel prior," *Neurocomputing*, vol. 149, pp. 1017–1026, 2015.

[30] J. Wang, K. Lu, J. Xue, N. He, and L. Shao, "Single image dehazing based on the physical model and msrcr algorithm," *IEEE Transactions on CSVT*, vol. 28, no. 9, pp. 2190–2199, 2017.

[31] D. Berman, T. Treibitz, and S. Avidan, "Single image dehazing using haze-lines," *IEEE TPAMI*, vol. 42, no. 3, pp. 720–734, 2018.

[32] J. Li, H. Zhang, D. Yuan, and M. Sun, "Single image dehazing using the change of detail prior," *Neurocomputing*, vol. 159, pp. 11–21, 2015.

[33] F. Yuan, Y. Zhou, X. Xia, X. Qian, and J. Huang, "A confidence prior for image dehazing," *Pattern Recognition*, vol. 119, p. 108076, 2021.

[34] Y. Feng, Z. Su, L. Ma, X. Li, R. Liu, and F. Zhou, "Bridging the gap between haze scenarios: A unified image dehazing model," *IEEE Transactions on CSVT*, 2024.

[35] X. Liu, H. Zhang, Y.-m. Cheung, X. You, and Y. Y. Tang, "Efficient single image dehazing and denoising: An efficient multi-scale correlated wavelet approach," *Computer Vision and Image Understanding*, vol. 162, pp. 23–33, 2017.

[36] Z. Li and J. Zheng, "Single image de-hazing using globally guided image filtering," *IEEE TIP*, vol. 27, no. 1, pp. 442–450, 2017.

[37] S. Ma, W. Pan, H. Liu, S. Dai, B. Xu, C. Xu, X. Li, and H. Guan, "Image dehazing based on improved color channel transfer and multiexposure fusion," *Advances in Multimedia*, vol. 2023, no. 1, p. 8891239, 2023.

[38] R. T. Tan, "Visibility in bad weather from a single image," in *CVPR*, 2008, pp. 1–8.

[39] A. Galdran, J. Vazquez-Corral, D. Pardo, and M. Bertalmio, "Enhanced variational image dehazing," *SIAM Journal on Imaging Sciences*, vol. 8, no. 3, pp. 1519–1546, 2015.

[40] B. Cai, X. Xu, K. Jia, C. Qing, and D. Tao, "Dehazenet: An end-to-end system for single image haze removal," *IEEE TIP*, vol. 25, no. 11, pp. 5187–5198, 2016.

[41] X. Liu, Y. Ma, Z. Shi, and J. Chen, "Griddehazenet: Attention-based multi-scale network for image dehazing," in *ICCV*, 2019, pp. 7314–7323.

[42] X. Zhang, T. Wang, J. Wang, G. Tang, and L. Zhao, "Pyramid channel-based feature attention network for image dehazing," *Computer Vision and Image Understanding*, vol. 197, p. 103003, 2020.

[43] Z. Zhu, H. Wei, G. Hu, Y. Li, G. Qi, and N. Mazur, "A novel fast single image dehazing algorithm based on artificial multiexposure image fusion," *IEEE Transactions on Instrumentation and Measurement*, vol. 70, pp. 1–23, 2020.

[44] P. Shyam, K.-J. Yoon, and K.-S. Kim, "Towards domain invariant single image dehazing," in *AAAI Conference on Artificial Intelligence*, vol. 35, no. 11, 2021, pp. 9657–9665.

[45] H. Bai, J. Pan, X. Xiang, and J. Tang, "Self-guided image dehazing using progressive feature fusion," *IEEE TIP*, vol. 31, pp. 1217–1229, 2022.

[46] A. Dudhane and S. Murala, "Ryf-net: Deep fusion network for single image haze removal," *IEEE TIP*, vol. 29, pp. 628–640, 2020.

[47] A. Dudhane, H. S. Aulakh, and S. Murala, "Ri-gan: An end-to-end network for single image haze removal," in *2019 IEEE/CVF Conference on CVPR Workshops*, 2019, pp. 2014–2023.

[48] M. Yu, T. Cui, H. Lu, and Y. Yue, "Vifnet: An end-to-end visible-infrared fusion network for image dehazing," *arXiv preprint arXiv:2404.07790*, 2024.

[49] D. Engin, A. Genç, and H. Kemal Ekenel, "Cycle-dehaze: Enhanced cyclegan for single image dehazing," in *CVPR workshops*, 2018, pp. 825–833.

[50] H. Zhu, X. Peng, V. Chandrasekhar, L. Li, and J.-H. Lim, "Dehazegan: When image dehazing meets differential programming." in *IJCAI*, 2018, pp. 1234–1240.

[51] A. Dudhane and S. Murala, "Cdnet: Single image de-hazing using unpaired adversarial training," in *WACV*. IEEE, 2019, pp. 1147–1155.

[52] W. Ren, J. Pan, H. Zhang, X. Cao, and M.-H. Yang, "Single image dehazing via multi-scale convolutional neural networks with holistic edges," *International Journal of Computer Vision*, vol. 128, pp. 240–259, 2020.

[53] P. Wang, H. Zhu, H. Huang, H. Zhang, and N. Wang, "Tms-gan: A twofold multi-scale generative adversarial network for single image dehazing," *IEEE Transactions on CSVT*, vol. 32, no. 5, pp. 2760–2772, 2021.

[54] Y. Wang, X. Yan, D. Guan, M. Wei, Y. Chen, X.-P. Zhang, and J. Li, "Cycle-snspgan: Towards real-world image dehazing via cycle spectral normalized soft likelihood estimation patch gan," *IEEE Transactions on ITS*, vol. 23, no. 11, pp. 20 368–20 382, 2022.

[55] C. M. Manu and K. Sreeni, "Ganid: a novel generative adversarial network for image dehazing," *The Visual Computer*, vol. 39, no. 9, pp. 3923–3936, 2023.

[56] Y. Song, Z. He, H. Qian, and X. Du, "Vision transformers for single image dehazing," *IEEE TIP*, vol. 32, pp. 1927–1941, 2023.

[57] W. Liu, Y. Cheng, and H. Qu, "Image self-enhancement de-hazing algorithm combined with generative adversarial network," *Journal of System Simulation*, vol. 36, no. 5, pp. 1093–1106, 2024.

[58] Y. Li, H. Chen, Q. Miao, D. Ge, S. Liang, Z. Ma, and B. Zhao, "Image hazing and dehazing: From the viewpoint of two-way image translation with a weakly supervised framework," *IEEE Transactions on Multimedia*, vol. 25, pp. 4704–4717, 2022.

[59] Y. Guo, Y. Gao, W. Liu, Y. Lu, J. Qu, S. He, and W. Ren, "Scanet: Self-paced semi-curricular attention network for non-homogeneous image dehazing," in *CVPR*, 2023, pp. 1885–1894.

[60] G. Kim, J. Park, and J. Kwon, "Deep dehazing powered by image processing network," in *CVPR*, 2023, pp. 1209–1218.

[61] H. Wei, Q. Wu, C. Wu, K. N. Ngan, H. Li, F. Meng, and H. Qiu, "Robust unpaired image dehazing via adversarial deformation constraint," *IEEE Transactions on CSVT*, 2024.

[62] J. Fu, S. Liu, Z. Liu, C.-L. Guo, H. Park, R. Wu, G. Wang, and C. Li, "Iterative predictor-critic code decoding for real-world image dehazing," in *CVPR*, June 2025, pp. 12 700–12 709.

[63] Y. Liu, X. Wang, E. Hu, A. Wang, B. Shiri, and W. Lin, "Vndhr: Variational single nighttime image dehazing for enhancing visibility in intelligent transportation systems via hybrid regularization," *IEEE Transactions on ITS*, pp. 1–15, 2025.

[64] L. Li, Y. Dong, W. Ren, J. Pan, C. Gao, N. Sang, and M.-H. Yang, "Semi-supervised image dehazing," *IEEE Transactions on Image Processing*, vol. 29, pp. 2766–2779, 2019.

[65] X. Cong, J. Gui, J. Zhang, and J. Hou, "A semi-supervised nighttime dehazing baseline with spatial-frequency aware and realistic brightness constraint," in *CVPR*, 2024.

[66] H. Wu, Y. Qu, S. Lin, J. Zhou, R. Qiao, Z. Zhang, Y. Xie, and L. Ma, "Contrastive learning for compact single image dehazing," in *CVPR*, 2021, pp. 10 551–10 560.

[67] Y. Yang, C. Wang, R. Liu, L. Zhang, X. Guo, and D. Tao, "Self-augmented unpaired image dehazing via density and depth decomposition," in *CVPR*, 2022, pp. 2037–2046.

[68] B. Ding, R. Zhang, L. Xu, G. Liu, and S. Yang, "U2d2net: Unsupervised unified image dehazing and denoising network for single hazy image enhancement," *IEEE TIP*, 2023.

[69] Y. Wang, X. Yan, F. Wang, and H. Xie, "Ucl-dehaze: Towards real-world image dehazing via unsupervised contrastive learning," *IEEE TIP*, 2024.

[70] Y. Park and T. Kim, "A video dehazing system based on fast airlight estimation," in *2017 IEEE Global Conference on Signal and Information Processing (GlobalSIP)*. IEEE, 2017, pp. 1185–1189.

[71] T. Dong, G. Zhao, J. Wu, Y. Ye, and Y. Shen, "Efficient traffic video dehazing using adaptive dark channel prior and spatial–temporal correlations," *Sensors*, 2019.

[72] S. Adidela, S. Singh, T. Sahu *et al.*, "Single image and video dehazing: A dark channel prior (dcp)-based approach," in *2021 IEEE 18th India Council International Conference (INDICON)*, 2021.

[73] X. Wu, X. Chen, X. Wang, X. Zhang, and S. Yuan, "A real-time framework for hd video defogging using modified dark channel prior," *Journal of Real-Time Image Processing*, 2024.

[74] B. Li, Y. Gou, J. Liu, H. Zhu, and J. Zhou, "Zero-shot image dehazing," *IEEE TIP*, 2020.

[75] K. Ashwini, H. Nenavath, and R. Jatoth, "Image and video dehazing based on transmission estimation and refinement using jaya algorithm," *Optik*, 2022.

[76] F. Yu, C. Qing, X. Xu, and B. Cai, "Image and video dehazing using view-based cluster segmentation," in *2016 Visual Communications and Image Processing (VCIP)*, 2016.

[77] P. Soma and R. Jatoth, "An efficient and contrast-enhanced video dehazing based on transmission estimation using hsl color model," *The Visual Computer*, 2022.

[78] J. Xu, X. Hu, L. Zhu, Q. Dou, and J. Dai, "Video dehazing via a multi-range temporal alignment network with physical prior," in *CVPR*, 2023.

[79] A. Ayoub, E. Naeem, and W. El-Shafai, "Video quality enhancement using dual-transmission-map dehazing," *Multimedia Tools and Applications*, 2024.

[80] J. Zhang, L. Li, Y. Zhang, G. Yang, X. Cao, and J. Sun, "Video dehazing with spatial and temporal coherence," *The Visual Computer*, vol. 27, no. 6, pp. 749–757, 2011.

[81] B. Cai, X. Xu, and D. Tao, "Real-time video dehazing based on spatio-temporal mrf," in *Pacific-Rim Conference on Multimedia*, 2016.

[82] M. Xue, Y. Ji, Z. Yuyan, and L. Weiwei, "Video image dehazing algorithm based on multi-scale retinex with color restoration," in *2016 International Conference on Intelligent Networking and Collaborative Systems (INCoS)*, 2016.

[83] V. M. Galshetwar, P. W. Patil, and S. Chaudhary, "Single frame-based video dehazing with adversarial learning," in *International Conference on Computer Vision and Image Processing*. Springer, 2021, pp. 36–47.

[84] V. M. Galshetwar, P. Patil, and S. Chaudhary, "Lrnet: Lightweight recurrent network for video dehazing," *Signal, Image and Video Processing*, vol. 17, no. 4, pp. 1475–1483, 2023.

[85] V. M. Galshetwar, P. Saini, and S. Chaudhary, "Drfnet: dual stream recurrent feature sharing network for video dehazing," *International Journal of Machine Learning and Cybernetics*, pp. 1–16, 2024.

[86] V. Galshetwar, P. Saini, and S. Chaudhary, "Cross-stage recurrent feature sharing network for video dehazing," *Expert Systems with Applications*, vol. 241, p. 122592, 2024.

[87] C. Ancuti, C. Ancuti, and F. Vasluianu, "Ntire 2023 hr nonhomogeneous dehazing challenge report," in *CVPR Worshop*, 2023.

[88] X. Liu, X. Min, W. Sun, and Y. Zhang, "Ntire 2023 quality assessment of video enhancement challenge," in *CVPR Workshop on NTIRE*, 2023.

[89] W. Yang, R. T. Tan, J. Feng, S. Wang, B. Cheng, and J. Liu, "Recurrent multi-frame deraining: Combining physics guidance and adversarial learning," *IEEE TPAMI*, vol. 44, no. 11, pp. 8569–8586, 2022.

[90] Y. Luo, Y. Xu, and H. Ji, "Removing rain from a single image via discriminative sparse coding," in *ICCV*, 2015.

[91] Y. Li, R. Tan, X. Guo, and J. Lu, "Rain streak removal using layer priors," in *CVPR*, 2016.

[92] S. Du, Y. Liu, M. Ye, Z. Xu, J. Li, and J. Liu, "Single image deraining via decorrelating the rain streaks and background scene in gradient domain," *Pattern Recognition*, 2018.

[93] H. Kim, S. Seo, and B. Song, "Multi-frame de-raining algorithm using a motion-compensated non-local mean filter for rainy video sequences," *Journal of Visual Communication and Image Representation*, 2015.

[94] V. Santhaseelan and V. Asari, "Utilizing local phase information to remove rain from video," *International Journal of Computer Vision*, 2015.

[95] A. Gautam and K. Raj, "Rain removal in digital images using guided filter," *Journal of Information Technology and Electrical Engineering*, 2018.

[96] W. Ren, J. Tian, Z. Han, and A. Chan, "Video desnowing and deraining based on matrix decomposition," in *CVPR*, 2017.

[97] P. Liu, C. Lin, C. Yeh, and L. Kang, "Rain removal using single image based on non-negative matrix factorization," in *Intelligent Systems and Applications*, 2015.

[98] X. Li, J. Wu, Z. Lin, H. Liu, and H. Zha, "Recurrent squeeze-and-excitation context aggregation net for single image deraining," in *ECCV*, 2018.

[99] S. Deng, M. Wei, J. Wang, and Y. Feng, "Detail-recovery image deraining via context aggregation networks," in *CVPR*, 2020.

[100] K. Jiang, Z. Wang, P. Yi, and C. Chen, "Multi-scale progressive fusion network for single image deraining," in *CVPR*, 2020.

[101] W. Yang, R. Tan, J. Feng, and J. Liu, "Deep joint rain detection and removal from a single image," in *CVPR*, 2017.

[102] H. Zhang, V. Sindagi, and V. Patel, "Image de-raining using a conditional generative adversarial network," *IEEE Transactions on CSVT*, 2019.

[103] Y. Wei, Z. Zhang, Y. Wang, M. Xu, and Y. Yang, "Deraincyclegan: Rain attentive cyclegan for single image deraining and rainmaking," *IEEE TIP*, 2021.

[104] X. Fu, B. Liang, Y. Huang, and X. Ding, "Lightweight pyramid networks for image deraining," *IEEE Transactions on Neural Networks and Learning Systems*, 2019.

[105] Q. Wang, G. Sun, J. Dong, and Y. Zhang, "Pfdn: Pyramid feature decoupling network for single image deraining," *IEEE TIP*, 2022.

[106] J. Xiao, X. Fu, A. Liu, F. Wu, and Z. Zha, "Image de-raining transformer," *IEEE TPAMI*, 2022.

[107] Y. Li, R. Lan, H. Huang, H. Zhou, Z. Liu, C. Pang, and X. Luo, "Single traffic image deraining via similarity-diversity model," *IEEE Transactions on ITS*, vol. 25, no. 1, pp. 90–103, 2024.

[108] J. Li, J. Hu, P. Fu, J. Yang, J. Jiang, and Y. Zhang, "Ultra-fast deraining plugin for vision-based perception of autonomous driving," *IEEE Transactions on ITS*, vol. 26, no. 1, pp. 1227–1240, 2025.

[109] M. R. Islam and M. Paul, "Video deraining using the visual properties of rain streaks," *IEEE Access*, vol. 10, pp. 202–212, 2022.

[110] Z. Mi, J. Shang, H. Zhou, and M. Wang, "Image fusion-based video deraining using sparse representation," *Electronics Letters*, 2016.

[111] A. Kulkarni, P. W. Patil, and S. Murala, "Progressive subtractive recurrent lightweight network for video deraining," *IEEE Signal Processing Letters*, vol. 29, pp. 229–233, 2022.

[112] S. Sun, W. Ren, J. Li, K. Zhang, M. Liang, and X. Cao, "Event-aware video deraining via multi-patch progressive learning," *IEEE Transactions on Image Processing*, vol. 32, pp. 3040–3053, 2023.

[113] Z. Yue, J. Xie, Q. Zhao, and D. Meng, "Semi-supervised video deraining with dynamical rain generator," in *CVPR*, 2021, pp. 642–652.

[114] W. Yang, J. Liu, and J. Feng, "Frame-consistent recurrent video deraining with dual-level flow," in *CVPR*, 2019, pp. 1661–1670.

[115] W. Yan, R. T. Tan, W. Yang, and D. Dai, "Self-aligned video deraining with transmission-depth consistency," in *CVPR*, 2021, pp. 11 966–11 976.
[116] J. Wang, W. Weng, Y. Zhang, and Z. Xiong, "Unsupervised video deraining with an event camera," in *ICCV*, 2023, pp. 10 831–10 840.
[117] D. Mao, S. Gao, Z. Li, H. Dai, Y. Zhang, and Y. Zhou, "Aggregating global and local representations via hybrid transformer for video deraining," *IEEE Transactions on CSVT*, 2024.
[118] B. Lin, Y. Jin, W. Yan, W. Ye, Y. Yuan, S. Zhang, and R. T. Tan, "Nightrain: Nighttime video deraining via adaptive-rain-removal and adaptive-correction," in *AAAI Conference on Artificial Intelligence*, vol. 38, 2024, pp. 3378–3385.
[119] H. Wu, Y. Yang, H. Xu, W. Wang, J. Zhou, and L. Zhu, "Rainmamba: Enhanced locality learning with state space models for video deraining," in *32nd ACM International Conference on Multimedia*, 2024, pp. 7881–7890.
[120] S. Sun, W. Ren, J. Zhou, S. Wang, J. Gan, and X. Cao, "Semi-supervised state-space model with dynamic stacking filter for real-world video deraining," in *CVPR*, June 2025, pp. 26 114–26 124.
[121] H. Chen, J. Ren, J. Gu, H. Wu, X. Lu, H. Cai, and L. Zhu, "Snow removal in video: A new dataset and a novel method," in *ICCV*, October 2023, pp. 13 211–13 222.
[122] K. Zhang, R. Li, Y. Yu, W. Luo, and C. Li, "Deep dense multi-scale network for snow removal using semantic and depth priors," *IEEE TIP*, vol. 30, pp. 7419–7431, 2021.
[123] W.-T. Chen, H.-Y. Fang, C.-L. Hsieh, C.-C. Tsai, I. Chen, J.-J. Ding, S.-Y. Kuo *et al.*, "All snow removed: Single image desnowing algorithm using hierarchical dual-tree complex wavelet representation and contradict channel loss," in *ICCV*, 2021, pp. 4196–4205.
[124] X. Ding, L. Chen, X. Zheng, Y. Huang, and D. Zeng, "Single image rain and snow removal via guided l0 smoothing filter," *Multimedia Tools and Applications*, 2016.
[125] F. Farhadifard and M. Radolko, "Single image marine snow removal based on a supervised median filtering scheme," in *VISIGRAPP (4 . . .*, 2017.
[126] H. Fan and H. Zhu, "Preservation of image edge feature based on snowfall model smoothing filter," *EURASIP Journal on Image and Video Processing*, 2018.
[127] H. Li, S. Liu, and Y. Piao, "Snow removal of video image based on fpga," in *5th International Conference on Electrical Engineering and Automatic Control*. Springer, 2016, pp. 207–215.
[128] Y. Zhan, J. Wang, J. Shi, and G. Cheng, "Distinguishing cloud and snow in satellite images via deep convolutional network," *IEEE Geoscience and Remote Sensing Letters*, 2017.
[129] Z. Li, J. Zhang, Z. Fang, B. Huang, X. Jiang, and Y. Gao, "Single image snow removal via composition generative adversarial networks," in *CVPR*, 2019.
[130] D.-W. Jaw, S.-C. Huang, and S.-Y. Kuo, "Desnowgan: An efficient single image snow removal framework using cross-resolution lateral connection and gans," *IEEE Transactions on CSVT*, vol. 31, no. 4, pp. 1342–1350, 2020.
[131] J. L. T Zhang, N Jiang, "Desnowformer: an effective transformer-based image desnowing network," in *ICIP*, 2022.
[132] S. Chen, T. Ye, Y. Liu, T. Liao, J. Jiang, E. Chen, and P. Chen, "Msp-former: Multi-scale projection transformer for single image desnowing," in *ICASSP*. IEEE, 2023, pp. 1–5.
[133] S. Chen, T. Ye, Y. Liu, and E. Chen, "Snowformer: Context interaction transformer with scale-awareness for single image desnowing," *arXiv preprint arXiv:2208.09703*, 2022.
[134] Y. Quan, X. Tan, Y. Huang, Y. Xu, and H. Ji, "Image desnowing via deep invertible separation," *IEEE Transactions on CSVT*, vol. 33, no. 7, pp. 3133–3144, 2023.
[135] J. Lai, S. Chen, Y. Lin, T. Ye, Y. Liu, S. Fei, Z. Xing, H. Wu, W. Wang, and L. Zhu, "Snowmaster: Comprehensive real-world image desnowing via mllm with multi-model feedback optimization," in *Proceedings of the Computer Vision and Pattern Recognition Conference (CVPR)*, June 2025, pp. 4302–4312.
[136] Y. Li, L. Wang, Z. Jia, J. Yang, and N. Kasabov, "Depth prior-based stable tensor decomposition for video snow removal," *Displays*, vol. 84, p. 102733, 2024.
[137] Y. Li, R. Wu, Z. Jia, J. Yang, and N. Kasabov, "Video desnowing and deraining via saliency and dual adaptive spatiotemporal filtering," *Sensors*, vol. 21, no. 22, p. 7610, 2021.
[138] T. Xue, G. Zhou, R. He, Z. Wang, J. Chen, and Z. Jia, "Rvdnet: a two-stage network for real-world video desnowing with domain adaptation," in *ICASSP*. IEEE, 2024, pp. 3305–3309.
[139] Y. Dong, W. Guo, M. Li, F. Zha, and B. Shao, "Framework of degraded image restoration and simultaneous localization and mapping for multiple bad weather conditions," *Optical Engineering*, 2023.
[140] D. Chen, M. He, Q. Fan, J. Liao, L. Zhang, D. Hou, L. Yuan, and G. Hua, "Gated context aggregation network for image dehazing and deraining," in *WACV*. IEEE, 2019, pp. 1375–1383.
[141] J. Zang, N. Xu, R. Liu, and Y. Shi, "Deraining and desnowing algorithm on adaptive tolerance and dual-tree complex wavelet fusion," *International Journal of Interactive Multimedia and Artificial Intelligence*, 2020.
[142] S. W. Zamir, A. Arora, S. Khan, M. Hayat, F. S. Khan, M.-H. Yang, and L. Shao, "Multi-stage progressive image restoration," in *CVPR*, 2021, pp. 14 821–14 831.
[143] A. Kulkarni, S. S. Phutke, and S. Murala, "Unified transformer network for multi-weather image restoration," in *ECCV*. Springer, 2022, pp. 225–240.
[144] S. W. Zamir, A. Arora, S. Khan, M. Hayat, F. S. Khan, and M.-H. Yang, "Restormer: Efficient transformer for high-resolution image restoration," in *CVPR*, 2022, pp. 5728–5739.
[145] Z. Wang, X. Cun, J. Bao, W. Zhou, J. Liu, and H. Li, "Uformer: A general u-shaped transformer for image restoration," in *CVPR*, 2022, pp. 17 683–17 693.
[146] M. Zhou, J. Huang, C.-L. Guo, and C. Li, "Fourmer: An efficient global modeling paradigm for image restoration," in *ICML*. PMLR, 2023, pp. 42 589–42 601.
[147] T. Gao, Y. Wen, K. Zhang, and J. Zhang, "Frequency-oriented efficient transformer for all-in-one weather-degraded image restoration," *IEEE Transactions on CSVT*, 2023.
[148] T. Wang, K. Zhang, Z. Shao, W. Luo, and B. Stenger, "Gridformer: Residual dense transformer with grid structure for image restoration in adverse weather conditions," *International Journal of Computer Vision*, 2024.
[149] J. Xu, M. Wu, X. Hu, C.-W. Fu, Q. Dou, and P.-A. Heng, "Towards real-world adverse weather image restoration: Enhancing clearness and semantics with vision-language models," in *ECCV*. Springer, 2024, pp. 147–164.
[150] H. Qin, W. Luo, L. Wang, D. Zheng, J. Chen, M. Yang, B. Li, and W. Hu, "Reversing flow for image restoration," in *CVPR*, June 2025, pp. 7545–7558.
[151] J. Kim, J. Sim, and C. Kim, "Video deraining and desnowing using temporal correlation and low-rank matrix completion," *IEEE TIP*, 2015.
[152] V. M. Galshetwar, A. Kulkarni, and S. Chaudhary, "Consolidated adversarial network for video de-raining and de-hazing," in *18th IEEE International Conference on AVSS*. IEEE, 2022, pp. 1–8.
[153] P. W. Patil, S. Gupta, S. Rana, and S. Venkatesh, "Dual-frame spatio-temporal feature modulation for video enhancement," *Pattern Recognition*, p. 108822, 2022.
[154] B. Li, W. Ren, D. Fu, D. Tao, D. Feng, W. Zeng, and Z. Wang, "Benchmarking single-image dehazing and beyond," *IEEE TIP*, vol. 28, no. 1, pp. 492–505, 2019.
[155] X. Qin, Z. Wang, Y. Bai, X. Xie, and H. Jia, "Ffa-net: Feature fusion attention network for single image dehazing," *AAAI Conference on AI*, vol. 34, pp. 11 908–11 915, Apr. 2020.
[156] X. Zhang, H. Dong, J. Pan, C. Zhu, Y. Tai, C. Wang, J. Li, F. Huang, and F. Wang, "Learning to restore hazy video: A new real-world dataset and a new method," in *CVPR*, 2021, pp. 9239–9248.
[157] C. O. Ancuti, C. Ancuti, M. Sbert, and R. Timofte, "Dense haze: A benchmark for image dehazing with dense-haze and haze-free images," in *IEEE International Conference on Image Processing*, ser. IEEE ICIP 2019, 2019.
[158] W. Luo, H. Qin, Z. Chen, L. Wang, D. Zheng, Y. Li, Y. Liu, B. Li, and W. Hu, "Visual-instructed degradation diffusion for all-in-one image restoration," in *CVPR*, June 2025, pp. 12 764–12 777.
[159] C. Ancuti, C. Ancuti, and R. Timofte, "Nh-haze: An image dehazing benchmark with non-homogeneous hazy and haze-free images," in *CVPRW*, 2020.
[160] S. Zhao, L. Zhang, S. Huang, Y. Shen, S. Zhao, and Y. Yang, "Evaluation of defogging: A real-world benchmark dataset, a new criterion and baselines," in *2019 IEEE International Conference on Multimedia and Expo (ICME)*, 2019, pp. 1840–1845.
[161] P. Ling, H. Chen, X. Tan, Y. Shan, and Y. Jin, "Single image dehazing using scene depth ordering," 2024.
[162] A. Filin, A. V. Kopylov, O. Seredin, and I. Gracheva, "Hazy images dataset with localized light sources for experimental evaluation of dehazing methods," *The 6th International Workshop on DLCP2022 — PoS*, 2022.

[163] Y. Jin, B. Lin, W. Yan, Y. Yuan, W. Ye, and R. T. Tan, "Enhancing visibility in nighttime haze images using guided apsf and gradient adaptive convolution," 2024.

[164] Y. Zhang, L. Ding, and G. Sharma, "Hazerd: An outdoor scene dataset and benchmark for single image dehazing," in *IEEE International Conference on Image Processing (ICIP)*, 2017, pp. 3205–3209.

[165] Y. Liu, L. Zhu, S. Pei, H. Fu, J. Qin, Q. Zhang, L. Wan, and W. Feng, "From synthetic to real: Image dehazing collaborating with unlabeled real data," in *ACM MM*, 2021.

[166] R. Ranftl, K. Lasinger, D. Hafner, K. Schindler, and V. Koltun, "Towards robust monocular depth estimation: Mixing datasets for zero-shot cross-dataset transfer," *IEEE TPAMI*, 2020.

[167] N. Silberman and R. Fergus, "Indoor scene segmentation using a structured light sensor," in *2011 IEEE ICCV Workshops*, 2011, pp. 601–608.

[168] C. Ancuti, C. Ancuti *et al.*, "D-hazy: A dataset to evaluate quantitatively dehazing algorithms," in *IEEE Conference on Image Processing*. IEEE, 2016.

[169] J. Gui, X. Cong, C. Peng, Y. Y. Tang, and J. T.-Y. Kwok, "Fooling the image dehazing models by first order gradient," *IEEE Transactions on CSVT*, vol. 34, no. 7, pp. 6265–6278, 2024.

[170] C. Ancuti, C. O. Ancuti, R. Timofte, and C. De Vleeschouwer, "I-haze: A dehazing benchmark with real hazy and haze-free indoor images," in *Advanced Concepts for Intelligent Vision Systems: 19th International Conference, ACIVS 2018, Poitiers, France, September 24–27, 2018, Proceedings 19*. Springer, 2018, pp. 620–631.

[171] R. Li, L.-F. Cheong, and R. T. Tan, "Heavy rain image restoration: Integrating physics model and conditional adversarial learning," in *2019 IEEE/CVF Conference on CVPR*, 2019, pp. 1633–1642.

[172] W. Yang, R. T. Tan, J. Feng, J. Liu, Z. Guo, and S. Yan, "Deep joint rain detection and removal from a single image," *CVPR*, pp. 1685–1694, 2016.

[173] D. Ren, W. Zuo, Q. Hu, P. Zhu, and D. Meng, "Progressive image deraining networks: A better and simpler baseline," in *2019 IEEE/CVF Conference on CVPR*, 2019, pp. 3932–3941.

[174] S. Li, I. B. Araujo, W. Ren, Z. Wang, E. K. Tokuda, R. H. Junior, R. Cesar-Junior, J. Zhang, X. Guo, and X. Cao, "Single image deraining: A comprehensive benchmark analysis," in *2019 IEEE/CVF Conference on CVPR*, 2019, pp. 3833–3842.

[175] X. Hu, C.-W. Fu, L. Zhu, and P.-A. Heng, "Depth-attentional features for single-image rain removal," in *CVPR*, 2019, pp. 8022–8031.

[176] Y. Park, M. Jeon, J. Lee, and M. Kang, "Mcw-net: Single image deraining with multi-level connections and wide regional non-local blocks," *Signal Processing: Image Communication*, vol. 105, p. 116701, 2022.

[177] Y. Li, R. T. Tan, X. Guo, J. Lu, and M. S. Brown, "Rain streak removal using layer priors," in *CVPR*, 2016, pp. 2736–2744.

[178] C. Yue, Z. Peng, J. Ma, S. Du, P. Wei, and D. Zhang, "Image restoration through generalized ornstein-uhlenbeck bridge," in *41st International Conference on Machine Learning*, ser. ICML'24. JMLR.org, 2024.

[179] X. Fu, J. Huang, D. Zeng, Y. Huang, X. Ding, and J. Paisley, "Removing rain from single images via a deep detail network," in *CVPR*, 2017, pp. 1715–1723.

[180] S. Yamashita and M. Ikehara, "Image deraining with frequency-enhanced state space model," in *ACCV*, December 2024, pp. 3655–3671.

[181] H. Zhang and V. M. Patel, "Density-aware single image de-raining using a multi-stream dense network," in *2018 IEEE/CVF Conference on CVPR*, 2018, pp. 695–704.

[182] B. Fu and H. Wang, "A single image deraining network based on global feature perception," in *6th International Conference on Computer Science and Artificial Intelligence*, ser. CSAI '22. Association for Computing Machinery, 2023, p. 81–86.

[183] T. Wang, X. Yang, K. Xu, and S. Chen, "Spatial attentive single-image deraining with a high quality real rain dataset," in *CVPR*, 2019.

[184] Y. Wang, C. Ma, and J. Liu, "Smartassign: Learning a smart knowledge assignment strategy for deraining and desnowing," in *CVPR*, June 2023, pp. 3677–3686.

[185] S. Zhou, D. Chen, J. Pan, J. Shi, and J. Yang, "Adapt or perish: Adaptive sparse transformer with attentive feature refinement for image restoration," in *CVPR*, 2024, pp. 2952–2963.

[186] A. Mittal, R. Soundararajan, and A. C. Bovik, "Making a "completely blind" image quality analyzer," *IEEE Signal Processing Letters*, vol. 20, no. 3, pp. 209–212, 2013.

[187] W.-T. Chen, H.-Y. Fang, J.-J. Ding, C.-C. Tsai, and S.-Y. Kuo, "Jstasr: Joint size and transparency-aware snow removal algorithm based on modified partial convolution and veiling effect removal," in *ECCV*. Springer, 2020, pp. 754–770.

[188] A. Ghasemabadi, M. K. Janjua, M. Salameh, and D. Niu, "Learning truncated causal history model for video restoration," *ArXiv*, vol. abs/2410.03936, 2024.

[189] Y.-F. Liu, D.-W. Jaw, S.-C. Huang, and J.-N. Hwang, "Desnownet: Context-aware deep network for snow removal," *IEEE TIP*, vol. 27, no. 6, pp. 3064–3073, 2018.

[190] K. Zhang, R. Li, Y. Yu, W. Luo, and C. Li, "Deep dense multi-scale network for snow removal using semantic and depth priors," *IEEE TIP*, vol. 30, pp. 7419–7431, 2021.

[191] V. Potlapalli, S. W. Zamir, S. H. Khan, and F. Shahbaz Khan, "Promptir: Prompting for all-in-one image restoration," *Advances in Neural Information Processing Systems*, vol. 36, pp. 71 275–71 293, 2023.

[192] D. Serrano-Lozano, L. Herranz, S. Su, and J. Vazquez-Corral, "Adaptive blind all-in-one image restoration," *arXiv preprint arXiv:2411.18412*, 2024.

[193] C. Li, F. Sun, H. Zhou, Y. Xie, Z. Li, and L. Zhu, "Multi-weather restoration: An efficient prompt-guided convolution architecture," *IEEE Transactions on CSVT*, vol. 35, no. 2, pp. 1436–1450, 2025.

[194] Y. Cui, S. W. Zamir, S. Khan, A. Knoll, M. Shah, and F. S. Khan, "Adair: Adaptive all-in-one image restoration via frequency mining and modulation," *arXiv preprint arXiv:2403.14614*, 2024.

[195] X. Tian, X. Liao, X. Liu, M. Li, and C. Ren, "Degradation-aware feature perturbation for all-in-one image restoration," in *CVPR*, June 2025, pp. 28 165–28 175.

[196] Z. Liu, S. Zhou, Y. Dai, Y. Wang, Y. An, and X. Zhao, "Dpmambair: All-in-one image restoration via degradation-aware prompt state space model," *arXiv preprint arXiv:2504.17732*, 2025.

[197] B. Cheng, J. Li, J. Shi, Y. Fang, G. Zhang, Y. Chen, T. Zeng, and Z. Li, "Weafu: Weather-informed image blind restoration via multi-weather distribution diffusion," *IEEE TCSVT*, vol. PP, pp. 1–1, 12 2024.

[198] Y. Jiang, Z. Zhang, T. Xue, and J. Gu, "Autodir: Automatic all-in-one image restoration with latent diffusion," in *ECCV*. Springer, 2024, pp. 340–359.

[199] R. Zhu, Z. Tu, J. Liu, A. C. Bovik, and Y. Fan, "Mwformer: Multi-weather image restoration using degradation-aware transformers," *IEEE TIP*, vol. 33, pp. 6790–6805, 2024.

[200] Y. Luo, R. Zhao, X. Wei, J. Chen, Y. Lu, S. Xie, T. Wang, R. Xiong, M. Lu, and S. Zhang, "Wm-moe: Weather-aware multi-scale mixture-of-experts for blind adverse weather removal," *arXiv preprint arXiv:2303.13739*, 2023.

[201] R. Li, R. T. Tan, and L.-F. Cheong, "All in one bad weather removal using architectural search," in *CVPR*, 2020, pp. 3175–3185.

[202] M. Siddiqua, S. B. Belhaouari, N. Akhter, and A. Zameer, "Macgan: An all-in-one image restoration under adverse conditions using multidomain attention-based conditional gan," in *IEEE TIP*, 2023, pp. 1–12.

[203] M. V. Conde, G. Geigle, and R. Timofte, "Instructir: High-quality image restoration following human instructions," in *ECCV*, 2024, p. 1–21.

[204] H. Yang, L. Pan, and Y. Yang, "Language-driven all-in-one adverse weather removal," in *CVPR*, 2024, pp. 214–224.

[205] W.-T. Chen, Z.-K. Huang, C.-C. Tsai, H.-H. Yang, J.-J. Ding, and S.-Y. Kuo, "Learning multiple adverse weather removal via two-stage knowledge learning and multi-contrastive regularization: Toward a unified model," in *CVPR*, 2022, pp. 17 653–17 662.

[206] Y. Zhu, T. Wang, X. Fu, X. Yang, X. Guo, J. Dai, Y. Qiao, and X. Hu, "Learning weather-general and weather-specific features for image restoration under multiple adverse weather conditions," in *CVPR*, 2023, pp. 21 747–21 758.

[207] B. Li, X. Liu, P. Hu, Z. Wu, J. Lv, and X. Peng, "All-in-one image restoration for unknown corruption," in *CVPR*, 2022, pp. 17 431–17 441.

[208] D. Eigen, D. Krishnan, and R. Fergus, "Restoring an image taken through a window covered with dirt or rain," in *ICCV*, 2013, pp. 633–640.

[209] Y. Qu, Y. Chen, J. Huang, and Y. Xie, "Enhanced pix2pix dehazing network," in *IEEE/CVF Conference on CVPR*, June 2019, pp. 8152–8160.

[210] R. Quan, X. Yu, Y. Liang, and Y. Yang, "Removing raindrops and rain streaks in one go," in *CVPR*, 2021, pp. 9147–9156.

[211] Y. Quan, S. Deng, Y. Chen, and H. Ji, "Deep learning for seeing through window with raindrops," in *ICCV*, 2019, pp. 2463–2471.

[212] X. Liu, M. Suganuma, Z. Sun, and T. Okatani, "Dual residual networks leveraging the potential of paired operations for image restoration," in *CVPR*, 2019, pp. 7007–7016.

[213] Z. Tu, H. Talebi, H. Zhang, F. Yang, P. Milanfar, A. Bovik, and Y. Li, "Maxim: Multi-axis mlp for image processing," in *CVPR*, 2022, pp. 5769–5780.

[214] T. Ye, S. Chen, J. Bai, J. Shi, C. Xue, J. Jiang, J. Yin, E. Chen, and Y. Liu, "Adverse weather removal with codebook priors," in *ICCV*, 2023, pp. 12 653–12 664.

[215] B. Cai, X. Xu, and D. Tao, "Real-time video dehazing based on spatio-temporal mrf," in *PCM*, 2016.

[216] M. Tassano, J. Delon, and T. Veit, "Fastdvdnet: Towards real-time deep video denoising without flow estimation," in *CVPR*, 2020, pp. 1354–1363.

[217] X. Liu, Y. Ma, Z. Shi, and J. Chen, "Griddehazenet: Attention-based multi-scale network for image dehazing," in *2019 IEEE/CVF ICCV*. IEEE Computer Society, 2019, pp. 7313–7322.

[218] B. Li, X. Peng, Z. Wang, J. Xu, and D. Feng, "End-to-end united video dehazing and detection," *arXiv preprint arXiv:1709.03919*, 2017.

[219] H. Dong, J. Pan, L. Xiang, Z. Hu, X. Zhang, F. Wang, and M.-H. Yang, "Multi-scale boosted dehazing network with dense feature fusion," in *2020 IEEE/CVF Conference on CVPR*, 2020, pp. 2154–2164.

[220] W. Ren, J. Zhang, X. Xu, L. Ma, X. Cao, G. Meng, and W. Liu, "Deep video dehazing with semantic segmentation," *IEEE TIP*, vol. 28, no. 4, pp. 1895–1908, 2019.

[221] S. Zhao, L. Zhang, Y. Shen, and Y. Zhou, "Refinednet: A weakly supervised refinement framework for single image dehazing," *IEEE TIP*, vol. 30, pp. 3391–3404, 2021.

[222] Y. Shao, L. Li, W. Ren, C. Gao, and N. Sang, "Domain adaptation for image dehazing," in *CVPR*, 2020, pp. 2808–2817.

[223] X. Wang, K. K. Chan, K. Yu, C. Dong, and C. Loy, "Edvr: Video restoration with enhanced deformable convolutional networks," in *2019 IEEE/CVF Conference on CVPR Workshops*. IEEE Computer Society, 2019, pp. 1954–1963.

[224] R. Li, "Progressive deep video dehazing without explicit alignment estimation," *CoRR*, vol. abs/2107.07837, 2021.

[225] J. Shin, H. Park, and J. Paik, "Region-based dehazing via dual-supervised triple-convolutional network," *IEEE Transactions on Multimedia*, vol. 24, pp. 245–260, 2022.

[226] J. Shin, M. Kim, J. Paik, and S. Lee, "Radiance–reflectance combined optimization and structure-guided l0-norm for single image dehazing," *IEEE Transactions on Multimedia*, vol. 22, no. 1, pp. 30–44, 2020.

[227] Z. Zhu, H. Wei, G. Hu, Y. Li, G. Qi, and N. Mazur, "A novel fast single image dehazing algorithm based on artificial multiexposure image fusion," *IEEE Transactions on Instrumentation and Measurement*, vol. 70, pp. 1–23, 2021.

[228] S. Dhara, M. Roy, D. Sen, and P. Kumar Biswas, "Color cast dependent image dehazing via adaptive airlight refinement and non-linear color balancing," *IEEE Transactions on CSVT*, vol. 31, no. 5, pp. 2076–2081, 2021.

[229] M. S. CO Ancuti, C Ancuti, "Dense-haze: A benchmark for image dehazing with dense-haze and haze-free images," in *IEEE International Conference on Image Processing (ICIP)*, 2019.

[230] R.-Q. Wu, Z.-P. Duan, C.-L. Guo, Z. Chai, and C. Li, "Ridcp: Revitalizing real image dehazing via high-quality codebook priors," in *CVPR*, 2023, pp. 22 282–22 291.

[231] B. Li, X. Peng, Z. Wang, J. Xu, and D. Feng, "Aod-net: All-in-one dehazing network," in *ICCV*, 2017, pp. 4770–4778.

[232] C.-L. Guo, Q. Yan, S. Anwar, R. Cong, W. Ren, and C. Li, "Image dehazing transformer with transmission-aware 3d position embedding," in *CVPR*, 2022, pp. 5812–5820.

[233] Y. Qiu, K. Zhang, C. Wang, W. Luo, H. Li, and Z. Jin, "Mb-taylorformer: Multi-branch efficient transformer expanded by taylor formula for image dehazing," in *ICCV*, 2023, pp. 12 802–12 813.

[234] H. Wang, Q. Xie, Q. Zhao, and D. Meng, "A model-driven deep neural network for single image rain removal," in *CVPR*, 2020, pp. 3100–3109.

[235] Q. Yi, J. Li, Q. Dai, F. Fang, G. Zhang, and T. Zeng, "Structure-preserving deraining with residue channel prior guidance," in *ICCV*, 2021, pp. 4218–4227.

[236] X. Fu, Q. Qi, Z.-J. Zha, and Y. Zhu, "Rain streak removal via dual graph convolutional network," *AAAI Conference on Artificial Intelligence*, vol. 35, pp. 1352–1360, 05 2021.

[237] D. Lin, X. WANG, J. Shen, R. Zhang, R. Liu, M. Wang, W. Xie, Q. Guo, and P. Li, "Generative status estimation and information decoupling for image rain removal," in *Advances in Neural Information Processing Systems*, vol. 35. Curran Associates, Inc., 2022, pp. 4612–4625.

[238] X. Fu, J. Xiao, Y. Zhu, A. Liu, F. Wu, and Z.-J. Zha, "Continual image deraining with hypergraph convolutional networks," *IEEE TPAMI*, vol. 45, no. 8, pp. 9534–9551, 2023.

[239] Y. Guo, X. Xiao, Y. Chang, S. Deng, and L. Yan, "From sky to the ground: A large-scale benchmark and simple baseline towards real rain removal," in *ICCV*, 2023, pp. 12 063–12 073.

[240] K. Purohit, M. Suin, A. Rajagopalan, and V. N. Boddeti, "Spatially-adaptive image restoration using distortion-guided networks," in *ICCV*, 2021, pp. 2309–2319.

[241] X. Chen, H. Li, M. Li, and J. Pan, "Learning a sparse transformer network for effective image deraining," in *CVPR*, June 2023, pp. 5896–5905.

[242] Z. Tan, Y. Wu, Q. Liu, Q. Chu, L. Lu, J. Ye, and N. Yu, "Exploring the application of large-scale pre-trained models on adverse weather removal," *IEEE TIP*, vol. 33, pp. 1683–1698, 2024.

[243] X. Zheng, Y. Liao, W. Guo, X. Fu, and X. Ding, "Single-image-based rain and snow removal using multi-guided filter," in *Neural Information Processing: 20th International Conference, ICONIP 2013, Daegu, Korea, November 3-7, 2013. Proceedings, Part III 20*. Springer, 2013, pp. 258–265.

[244] W.-T. Chen, H.-Y. Fang, J.-J. Ding, C.-C. Tsai, and S.-Y. Kuo, "Jstasr: Joint size and transparency-aware snow removal algorithm based on modified partial convolution and veiling effect removal," in *ECCV*. Springer, 2020, pp. 754–770.

[245] Y. Liu, Z. Qin, S. Anwar, P. Ji, D. Kim, S. Caldwell, and T. Gedeon, "Invertible denoising network: A light solution for real noise removal," in *CVPR*, 2021, pp. 13 365–13 374.

[246] Y. Cheng, H. Ren, R. Zhang, and H. Lu, "Context-aware coarse-to-fine network for single image desnowing," *Multimedia Tools and Applications*, pp. 1–18, 2023.

[247] C. Tian, Y. Xu, and W. Zuo, "Image denoising using deep cnn with batch renormalization," *Neural Networks*, vol. 121, pp. 461–473, 2020.

[248] H. Gao, X. Tao, X. Shen, and J. Jia, "Dynamic scene deblurring with parameter selective sharing and nested skip connections," in *CVPR*, 2019, pp. 3843–3851.

[249] Y. Dong, Y. Liu, H. Zhang, S. Chen, and Y. Qiao, "Fd-gan: Generative adversarial networks with fusion-discriminator for single image dehazing," in *AAAI Conference on Artificial Intelligence*, 2020.

[250] Q. Fan, D. Chen, L. Yuan, G. Hua, N. Yu, and B. Chen, "A general decoupled learning framework for parameterized image operators," *IEEE TPAMI*, vol. 43, no. 1, pp. 33–47, 2021.

[251] E. Zamfir, Z. Wu, N. Mehta, Y. Tan, D. P. Paudel, Y. Zhang, and R. Timofte, "Complexity experts are task-discriminative learners for any image restoration," in *CVPR*, June 2025, pp. 12 753–12 763.

[252] Y. Gu, Y. Meng, J. Ji, and X. Sun, "Acl: Activating capability of linear attention for image restoration," in *CVPR*, June 2025, pp. 17 913–17 923.

[253] S. Chaudhary and S. Murala, "Depth-based end-to-end deep network for human action recognition," *IET Computer Vision*, vol. 13, no. 1, pp. 15–22, 2019.

[254] S. Chaudhary and S. M., "Deep network for human action recognition using weber motion," *Neurocomputing*, vol. 367, pp. 207–216, 2019.

[255] P. Hambarde, S. Murala, and A. Dhall, "Uw-gan: Single-image depth estimation and image enhancement for underwater images," *IEEE Transactions on Instrumentation and Measurement*, vol. 70, pp. 1–12, 2021.

[256] P. Hambarde, A. Dudhane, and S. Murala, "Single image depth estimation using deep adversarial training," in *2019 IEEE International Conference on Image Processing (ICIP)*. IEEE, 2019, pp. 989–993.

[257] S. Chaudhary and S. Murala, "Tsnet: deep network for human action recognition in hazy videos," in *2018 IEEE International Conference on Systems, Man, and Cybernetics (SMC)*. IEEE, 2018, pp. 3981–3986.

[258] X. Wang, X. Liu, H. Yang, Z. Wang, X. Wen, X. He, L. Qing, and H. Chen, "Degradation modeling for restoration-enhanced object detection in adverse weather scenes," *IEEE Transactions on Intelligent Vehicles*, pp. 1–17, 2024.

[259] C. Li, H. Zhou, Y. Liu, C. Yang, Y. Xie, Z. Li, and L. Zhu, "Detection-friendly dehazing: Object detection in real-world hazy scenes," *IEEE TPAMI*, vol. 45, no. 7, pp. 8284–8295, 2023.

[260] P. Hambarde and S. Murala, "S2dnet: Depth estimation from single image and sparse samples," *IEEE Transactions on Computational Imaging*, vol. 6, pp. 806–817, 2020.

[261] K. Zhu, J. Gu, Z. You, Y. Qiao, and C. Dong, "An intelligent agentic system for complex image restoration problems," *arXiv preprint arXiv:2410.17809*, 2024.